Robust Control of a Wind Turbine Using Third Generation CRONE Control

Francisco Serpa Carvalho Ravasco

Thesis to obtain the Master of Science Degree in

Mechanical Engineering

Supervisors: Prof. Duarte Pedro Mata de Oliveira Valério
Prof. Mário Rui Melício da Conceição

Examination Committee

Chairperson: Prof. Paulo Jorge Coelho Ramalho Oliveira
Supervisor: Prof. Mário Rui Melício da Conceição
Member of the Committee: Dr. Nelson António Martins da Costa Batista

November 2018

To my brother and sister...

Acknowledgments

First and foremost, I would like to express my gratitude to my supervisors, Prof. Duarte Valério and Prof. Rui Melício, for their support and cooperation throughout this project, and for their valuable guidance.

I would like to thank to Sr. Raposeiro and Eng. Camilo Christo, for their availability and good will, helping me through the more practical work.

To my friends, I owe my gratitude for the company and the good times spent during this journeys, and for the encouragement, in times not so good. In particular, Eduardo Dunões, João Rodrigues and Daniel Fernandes, for accompanying me throughout this final project.

Finally, I would like to thank my family. My grandparents, for having me at their home during these years and for the patience they had. To my father and mother, for supporting me, never letting me down and always showing me the good side of what I was doing, always encouraging me to exceed myself. To my brother and sister, for making any time a wonderful one. And my girlfriend Marta for being always there for me, even when the studies did not let me be there for her.

Resumo

A presente dissertação foca-se na análise, desenvolvimento e simulação de um controlador CRONE de terceira geração a ser implementado num protótipo de uma nova turbina eólica de eixo vertical *Darrieus*.

O protótipo é composto por um rotor vertical com cinco asas rotativas e um gerador síncrono de ímanes permanentes. Este protótipo foi estudado, e os diferentes modelos, propostos em estudos anteriores, foram analisados. Dados experimentais do protótipo, adquiridos em projetos anteriores, foram estudados, e é proposta uma gama de *TSR* que melhor descreve o protótipo. A metodologia de *design* de sistemas de controlo CRONE foi abordada, e um controlador CRONE de terceira geração foi desenvolvido para o modelo que melhor descreve o comportamento do protótipo.

O modelo selecionado (*nominal plant*), foi usado para produzir mais dois modelos (*extreme plants 1 e 2*), que introduzem $\pm 20\%$ de incerteza nos coeficientes da função de transferência da *nominal plant*. O controlador CRONE foi testado em simulação, quando aplicado a cada uma das três plantas, em diferentes condições de vento, com e sem a presença de turbulência. O comportamento do controlador é apresentado e analizado, recorrendo a dois índices usados na literatura: o *ITAE* e o *ISV*.

Um conjunto de sensores e actuadores, integrados com uma plataforma *Arduino*, são propostos, foram desenvolvidos para o protótipo, e testes reais foram efectuados. O primeiro para validar os resultados obtidos, quanto à gama de *TSR* do protótipo, e o segundo para quantificar as limitações que a presença dos actuadores impõe, no comportamento do *TSR* do protótipo.

Palavras-chave: Energia Eólica; Turbina Eólica Darrieus; Protótipo; Estratégia de Controlo; Controlo Fraccionário; Controlo CRONE de Terceira Geração...

Abstract

This dissertation focuses on the analysis, development and simulation of a fractional-complex third generation CRONE controller to be implemented on a new Darrieus VAWT prototype.

The vertical axis wind turbine prototype comprises five rotary-wings (blades) and a permanent magnet synchronous generator. The prototype is studied, and its numerous dynamic models, proposed in previous works, are analysed. Previously acquired experimental data from the prototype is studied, and a new, more truthful TSR range is proposed. The CRONE control system design methodology is studied, and a controller is developed, for the model that better describes the prototype's behaviour.

The model selected (nominal plant), is used to produce two more models (extreme plants, 1 and 2), that introduce $\pm 20\%$ uncertainty in the nominal plant's transfer function coefficients. The CRONE controller is tested in simulation, when applied to each of the three plants, in different wind conditions, with and without the presence of turbulence. The controller's performance is presented and analysed, resorting to two metrics used in the literature: the ITAE and the ISV.

A set of sensors and actuators integrated with the *Arduino* platform, are proposed and built for the prototype, and two tests are performed. One, to validate the TSR range proposed at the beginning of the document, and another, to assess the limitations imposed by the actuator in the prototype's TSR behaviour.

Keywords: Wind Energy; Darrieus Wind Turbines; Prototype; Control Strategy; Fractional Control; Third Generation CRONE Control

Contents

List of Tables

List of Figures

Nomenclature

Greek symbols

β	Pitch Angle
$\delta\omega$	Rotor Angular Speed Variation
λ	Tip Speed Ratio
λ_0	Permanent Magnetic Flux
λ_{max}	Maximum Tip Speed Ratio
λ_{opt}	Optimal Tip Speed Ratio
ω	Rotor Angular Speed
ω_g	Generator Angular Speed
$\overline{\omega}$	Nominal Rotor Angular Speed
ρ	Air Density

Roman symbols

δi_i	Current Intensity Variation (i-axis)
δR_c	Circuit Resistance Variation
δT_a	Aerodynamic Torque Variation
δu_i	Tension Variation (i-axis)
δv	Wind Speed Variation
$\overline{i_i}$	Nominal Current Intensity (i-axis)
$\overline{R_c}$	Nominal Circuit Resistance
$\overline{T_a}$	Nominal Aerodynamic Torque
$\overline{u_i}$	Nominal Tension (i-axis)
$\overline{v}$	Nominal Wind Speed

A	Swept Area
c	Blade Profile Chord
C_p	Coefficient of Power
H	Rotor Height
i_i	Current Intensity (i-axis)
J_t	Moment of Inertia
L_i	Inductance (i-axis)
n_p	Number of Poles
P_{mec}	Mechanical Power
P_{wind}	Wind Power
R	Resistance
r	Rotor Radius
R_a	Armature Resistance
R_c	Circuit Resistance
T_a	Aerodynamic Torque
u_i	Tension (i-axis)
v	Wind Speed
Z	Number of Blades

Glossary

AC	Alternating Current
CFD	Computational Fluid Dynamics
CRONE	*Commande Robuste d'Ordre Non Entier*
CSD	Control System Design
DC	Direct Current
HAWT	Horizontal Axis Wind Turbine
IDE	Integrated Development Environment
LQR	Linear Quadratic Regulator
ODGV	Omni-Directional-Guiding-Vane
PID	Proportional Integer Derivative
PMSG	Permanent Magnet Synchronous Generator
PWM	Pulse Width Modulation
SCADA	Supervisory Control and Data Acquisition
TSR	Tip Speed Ratio
VAWT	Vertical Axis Wind Turbine

Chapter 1

Introduction

1.1 General Introduction

Since early days, mankind have harnessed the energy of the wind. Evidences of wind propelled boats from as early as 6000 B.C., have been found in the Arabian Gulf (Figure 1.1(a)) [1]. For many centuries, sailing boats were the transport that impelled civilizations to explore the world, exchanging goods and knowledge, contributing to the humanity's development. The earliest known windmills refer to wind-powered water pumps used in China, and, at around the same time, vertical-axis windmills with woven reed blades were grinding cereals in Persia and the Middle East (Figure 1.1(b)).

(a) Arabian Gulf Sailing Boat Reconstruction.

(b) Persian Vertical Axis Windmill.

Figure 1.1: First Known Usage of Wind's Energy.

New, more efficient designs have been developed since the first windmills, eventually merchants and crusaders carried this idea to Europe, where the Dutch have refined and adapted it for draining lakes and marshes in the Rhine River Delta. In the late 19th as part of the industrialization, the first windmill to generate electricity was built.

Presently, several different usages have been found for wind power. In the last two decades, impelled by a growing awareness on environmental issues, companies and governments have been considering alternatives to substitute the finite and highly pollutant fossil fuel resources. Powered by the need, wind turbines are now considered one of the most conspicuous energy sources. According to *GWEC*, the new installations in 2017 represented $52489\,\mathrm{MW}$, rising the global total installed wind capacity to $539123\,\mathrm{MW}$ [2]. In Figure 1.2 is noticeable the evolution with a growth over 2000% in the last sixteen years.

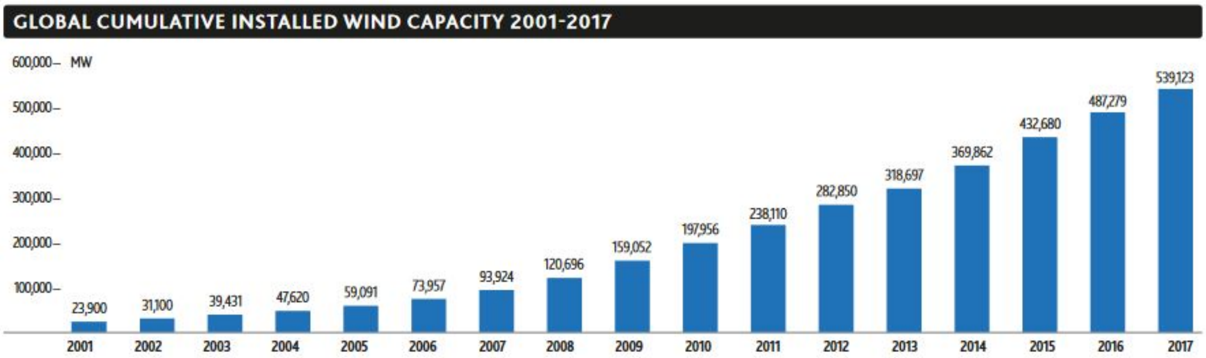

Figure 1.2: Global Cumulative Installed Wind Capacity 2001-2017 [2].

In 2017 wind energy generated in the EU-28's was enough to meet 11.6% of it's electricity demand. Leaded by Denmark with a penetration rate of 44%, followed by Portugal and Ireland both with 24%. In the EU-28's, 10 out of the 28 Member States had a wind penetration rate of more than 10%.

These data is clear on showing the future of wind energy production as part of a global energy plan for years to come. The currently available wind turbines are not perfect, and every year new models arrive to the market with more efficient blade profiles, more robust control strategies, and covering a wider range of winds and locations. Being a technology in permanent development there are different pros and cons that must be taken into account.

Wind Energy Advantages

- Infinite, sustainable and renewable source of energy;
- Competitive renewable energy source;
- Wind is distributed widely all over the world, providing opportunity for either develop and underdeveloped countries to have independent source of energy;
- Wildlife friendly, minimal ecological impact in the areas where installed;
- Low risks and low concerning regarding natural disasters, as wind farms tend to be installed in inhabited surroundings;
- Relatively low energy payback period (5 to 8 months on $2MW$ wind turbines [3]).

Wind Energy Disadvantages

- Large components (Blades, Tower, Nacelle) makes it difficult to install in remote locations, requiring exceptional transport and complex logistics;
- Long periods without energy conversion, either due to low wind speeds or excessive wind that could damage the turbine;

- Noise pollution, however it is not an issue for wind farms distant from civilization, it impossibilitates the production of energy closer to the final consumer;
- Visual impact in the rural landscapes;
- Main production hours tend to be at night time, also when the consumption is smaller, creating the necessity for storing energy and complement wind production with an alternative form of energy production (solar cells, hydro power).

(a) Horizontal Axis Wind Turbine (HAWT)

(b) Vertical Axis Wind Turbine (VAWT)

Figure 1.3: Examples of Different Wind Turbines

Nowadays the vast majority of wind turbines installed are Horizontal Axis Wind Turbines (HAWT)(Figure 1.3(a)). This implies that the energy is produced far from the final user, inducing more costs, as, due to the noise production and visual impact, this technology is not suited to urban environment. The solution may pass through Vertical Axis Wind Turbines (VAWT)(Figure 1.3(b)), resorting to a larger number of turbines spread over each city, producing decentralized electricity in a Smart Grid context. Even though they are behind HAWT in development and investment, VAWT present several advantages [4]:

- Insensitivity to yaw wind direction;
- Smaller number of components;
- Low sound emission;
- Ability to produce energy from wind in skewed flows;
- Capable of operating closer to the ground level;
- Generator position closer to the ground level, allowing for an easier maintenance.

There are two main types of VAWT, Darrieus and Savonius. All typical VAWT are composed by the same subsystems:

- **Rotor:**
  The rotor consists of the hub and blades of the turbine. The blades are considered the most important component of a wind turbine as they are responsible for the aerodynamics interaction with the wind, from which the performance is largely dependant.
- **Drive train:**
  The drive train is responsible for the coupling between the rotor and the generator. This is typically constituted by a low speed shaft integral with the rotor, a high speed shaft integral with the generator, and a gearbox.
- **Generator:**
  The generator is the component responsible for transforming the mechanical power in electricity. The most common are induction or synchronous generators.
- **Tower:**
  The tower is a key component, not only is the main frame of the wind turbine, responsible for maintaining all the other components together, it also has to be correctly dimensioned to support cyclic loads and to reduce the vibration between the rotor and the tower [5].
- **Controls:**
  The control system of a wind turbine is responsible for keeping the performance at optimum levels, monitoring the operating conditions and intervene accordingly either to increase the performance or to prevent eventual failures. This subsystem includes the following components:
  - **Sensors:** Responsible for the measurement of important quantities such as rotor speed, wind speed, current, voltage, strains in different structural components, etc;
  - **Controllers:** Mechanical mechanisms such as emergency brake and electrical circuits;
  - **Actuators:** The components that will actually manipulate the turbine's characteristics, examples are motors, potentiometers, magnets;
  - **Intelligence:** Computers, microprocessors, embedded systems, and all the hardware that performs the computational processes.

1.2 Objectives

In the context described, the main purpose of this work is to develop a third generation CRONE controller for a VAWT prototype, and verify its application in a real environment. To achieve this main objective several smaller objectives have to be accomplished:

- Study and analyse the VAWT prototype developed in [6];

- Study, analyse and verify the different prototype models proposed in [7];
- Develop a third generation CRONE controller for the model selected, resorting to the CRONE Control System Design Toolbox;
- Validate the controller in simulation in different wind conditions;
- Develop hardware and software to allow the implementation of the controller in the real prototype while collecting data for further analysis;
- Study and analyse the prototype's behaviour in a wind tunnel to unveil the TSR for which it presents the maximum coefficient of power;
- Test the controller in real environment analysing the prototype's performance.

1.3 State of the Art

The present State of the Art will focus on developments that have been made regarding Vertical Axis Wind Turbines, enlightening in subjects as design and product development, modelling, applicability, and identification and control strategies. The evolution of the CRONE control principles will also be addressed as well as different applications studied for this type of controller.

1.3.1 Darrieus VAWT Development Modelling an Control

The evolution of the Darrieus VAWT and an overview on the different types of VAWT is presented in [8]. The drawbacks and advantages of each Darrieus vertical axis wind turbines configuration are exploited.

In [9] the energetic suitability of a Darrieus VAWT installation in the rooftop of a building in an urban area is evaluated. The flow field in the rooftop area is characterized by means of numerical CFD analysis for different geometry buildings and numerous wind profiles. A numerical model has been developed to account for the effects of skewed flows on the power performance of the Darrieus rotor.

As studied in [10] a modern adaptation of the vertical axis Sistan type windmill (the oldest known windmill) can still compete with the new VAWT designs. Theoretical and scale model tests indicated that efficiencies higher than 40% can be expected. A design is also proposed that keeps the visual impact to a minimum and allows the integration of this type of wind turbines in current building architecture.

In [11] an omni-directional-guide-vane (ODGV) is studied for surrounding a VAWT when integrated in an urban high-rise building. The experimental results show an increase by about 125% in rotational speed, and a torque output increase by 206%, for a single bladed VAWT. Contributing for a performance growth without compromising the VAWT independence from wind direction or having a negative influence on visual impact.

A wireless monitoring computational framework of sensors, data acquisition, data processing and storage system is proposed in [12]. A low powered wireless network employing ZigBee protocol is used to ensure connectivity between the sensor modules. A voltage and current sensor, and an infrared photoelectric sensor for a VAWT are succinctly described.

In [6], [4] and [13] a Darrieus VAWT prototype is developed, featuring a new blade profile that provides the turbine capability for self-start. Numerous field tests are presented, concluding that the new design guarantees a self-start for wind velocities of $1.25\ \mathrm{m/s}$ exhibiting a stable behaviour under stress for winds with up to $25\ \mathrm{m/s}$, maintaining a good performance. The study and development of this new Darrieus type vertical axis rotary-wings is continued in [14], with the presentation of VAWT performance prediction models. The integration of this particular VAWT in urban context is approached, including self-start tests, noise production assessment and predictions in different types of turbulent and unstable wind behaviours that are common in urban areas.

In [15] and [16] two patents are presented for the prototype blades, in Portugal and the United States respectively.

Two theoretical models for the prototype are proposed in [7] and [17] along with different identified models. A PID controller and an LQR are developed and tested in simulation using the models previously developed. In the present document, the models formulated in [7] will be analysed, and used for the controller synthesis and simulation tests.

A model is proposed in [18] for wind energy systems simulation. The proposed model, which considers variable-speed wind turbine, two mass rotor, permanent magnet synchronous generator (PMSG) and different power converters, is more accurate and realistic. The publication also proposes a new control strategy based on fractional-order controllers. Simulation results show that the proposed control strategy improves disturbance attenuation and system robustness.

In [19] different control strategies for VAWT are analysed. It is also proposed a control technique for a sensorless application, maximizing the output power up to the rated wind speed when an anemometer is not available. The results are verified in a simulation environment using a *Simulink* equivalent model of a VAWT.

A hierarchical controller structure for wind energy conversion systems is presented in [20]. The hierarchy is composed by an event based supervisor in the higher level and two options for distinct controllers in the lower level: fuzzy PI and fractional-order PI, acting on the pitch angle of the blades. The simulation results for closed-loop response unveil the fact that the fuzzy PI controller outperforms the fractional-order PI, by its capability to deal with system nonlinearities and uncertainties, at a cost of a higher control effort. With the fractional-order PI allowing a reduction on the switches between operational states, but at expense of an oscillatory closed-loop response.

In [21] is presented a simulation of an onshore wind energy conversion system under an event-based supervisor control based on a finite state machine. Mathematical models of variable speed wind turbine with pitch control are studied, and different controllers are tested such as predictive control and adaptive control. The objective is to control the electric output power for around the reference power, and also to analyse the operational states according to the wind speed. The influence of the supervisory strategy on the performance is assessed by comparing the performance with or without the supervisory strategy.

A complete analysis including VAWT modelling, control development and implementation is presented in [22]. A supervisory control and data acquisition system (SCADA) is used to monitor and command the VAWT, and different algorithms and control strategies are studied. Performance test were also ran to investigate the turbine's optimum Cp as this curve was unknown.

1.3.2 CRONE Control

The CRONE control began being presented to the scientific community in [23] where the principles of the first generation CRONE control were stated. This control strategy is presented as being based on a recursive synthesis which provides a constant phase, and lead to a constant first overshoot, maintaining its robustness even when the plant's parameters are slightly changed. A comparison between the CRONE control and the PID control highlights the fact that the first remains efficient when the transitional frequency varies, even though the second stops being effective.

The CRONE research team proceeded the investigation, presenting the second generation CRONE controller in [24]. In this generation the template is a vertical straight line segment that the open-loop Nichols locus forms for the nominal parametric state of the plant. A vertical sliding of the template at the time of a plant reparametrization then ensures the constancy of resonance ratio and of the damping ratio of the control. The template is described by a real non integer integrator transmittance whose order determines its phase position.

Finally, in [25] the third generation CRONE controller is presented. This generation represents the generalization of the first two approaches. Based on the complex non integer derivation, the generalized template is defined, this time an indifferent direction straight line segment. Then, a performance criterion is established to select an optimal template that ensures the robustness of the controller within its uncertainty domain.

Numerous applications have been developed for the CRONE control. For example, in [26] the control of resonant plants is addressed. Dealing with a flexible transmission benchmark, significant modifications are provided to control the resonant modes of the plant.

More recently, a toolbox was developed by the CRONE research group, in [27] the toolbox for *Matlab* is presented along with a tutorial and a case study to simplify the usage among the engineer community. A manual for the toolbox was released [28], including the principles of all three generations of CRONE control, and explaining, resorting to examples and case studies, the toolbox functioning.

Although the CRONE Control System Design toolbox for *Matlab* allows optimizing the parameters of robust controllers, the performance of the optimized controllers highly depends on the experience of the user that sets the specifications. With this in mind, a new optimization criteria for the facilitating the design of third generation CRONE controllers is presented in [29]. A benchmark example is used to show that these criteria can be considered for a significant improvement in the use of CRONE CSD toolbox.

Chapter 2

Background

2.1 Vertical Axis Wind Power Generator

For better understanding the work done previously, to which the present document follows up, it is important to address the basic principles behind the mechanical and electrical models affine to wind turbines. This section will enlighten the reader on the basic dynamic equations governing the physical quantities of interest in this technology.

2.1.1 Non-linear Model

Turbine

The equations presented in this section are stated in various articles, the line of thought followed in this section is based in [30].

The main goal of a wind turbine is to convert the kinetic energy available in the wind into mechanical energy with the minimum losses possible. The power P available in an air flow with a mass density ρ at velocity v passing through an area A is given by:

$$P = \frac{1}{2}\rho A v^3 \tag{2.1}$$

Noticing that the projected area of a VAWT's rotor is computed as:

$$A = 2rH \tag{2.2}$$

being r the rotor radius and H the blade's height. The power P_{wind} contained in the wind passing through the turbines rotor is given by:

$$P_{wind} = \rho r H v^3 \tag{2.3}$$

However, not all the energy present in the wind flow can be availed, as not all the particles present in the flow end up touching the blades, and even the ones that do still conserve a part of the initial kinetic energy. The power coefficient (C_P) quantifies how much of the energy available in the wind is effectively converted in mechanical power by the turbine.

The C_P is expressed as a function of the tip speed ratio λ and the blade's pitch angle β, and is given by:

$$C_P(\lambda, \beta) = \frac{ExtractedPower}{AvailablePower} = \frac{P_{mec}}{P_{wind}} \tag{2.4}$$

Theoretically the power coefficient never surpasses the value of 0.593, as stated by Albert Betz in [31], in conclusion to a study that proved that no wind turbine can capture more than $59,3\%$ of the wind's kinetic energy; this limit is known as the Betz limit .

The interaction between the rotor and the wind stream is made resorting to a parameter called tip speed ratio λ. The tip speed ratio (TSR) is defined as the ratio between the linear velocity of the tip of the blade and the wind speed, and its given by:

$$\lambda = \frac{\omega r}{v} \tag{2.5}$$

In a HAWT it is clear that the TSR is measured at the tip of the blade; for a VAWT the tip of the blade position relative to the turbine axis is much dependant on the design of the turbine. Therefore, as in the VAWT considered, the blade's tips are closer to the axis than the middle section of the blade, the TSR is calculated at the middle section.

The aerodynamic power captured by the VAWT can be expressed as:

$$P_a = \frac{1}{2}\rho A C_P(\lambda) v^3 = \omega T_a \tag{2.6}$$

where A is the swept area of the rotor, λ the tip speed ratio (TSR), defined respectively by (2.2) and (2.5). T_a is the aerodynamic torque, obtained by rearranging (2.6) and defined by:

$$T_a = \rho r^2 H C_P(\lambda) v^2 \frac{1}{\lambda} \tag{2.7}$$

In section 2.2.3 the power coefficient function $C_P(\lambda)$ will be addressed in detail.

Permanent Magnet Synchronous Generator

The permanent magnet synchronous generator (PMSG) is responsible for converting the mechanical power captured by the rotor into electric power. The PMSG installed in the prototype considered in this document consists of a three phase AC generator with a generated magnetic field on the rotor and a stationary armature containing multiple windings.

The electrical model of the PMSG in the synchronous reference frame presented in [32] and adapted for this particular case in [17] is given by:

$$\frac{di_d}{dt} = -\frac{R_a}{L} i_q - \omega_g \left(i_d + \frac{1}{L}\lambda_0 \right) + \frac{1}{L} u_q \tag{2.8a}$$

$$\frac{di_q}{dt} = -\frac{R_a}{L} i_d + \omega_g i_q + \frac{1}{L} u_d \tag{2.8b}$$

where i_i and u_i are the current and voltage in the i-axis respectively, R_a is the armature resistance, ω_g is the generator angular speed and λ_0 is the permanent magnetic flux produced by the rotor magnets. $L = L_q = L_d$ are the summation of the inductances of the generator and the transformer, which simplification resulted in (2.8).

The generator angular speed ω_g is related to the turbine angular speed ω by the generator's number of poles n_p, in the form:

$$\omega_g = n_p \omega \tag{2.9}$$

The electromagnetic torque T_{em} produced by the generator, considering the simplifications introduced in (2.8) is given by:

$$T_{em} = \frac{3}{2} n_p \lambda_0 i_q \tag{2.10}$$

Experiments performed in [7] for this particular PMSG concluded that both phase tension and current present a direct proportional relation to the angular speed ω. The behaviour can be expressed by the following relations:

$$U(\omega) = 0.2841\,\omega + 0.2193 \quad (V) \tag{2.11a}$$

$$I(\omega) = 0.0089\,\omega - 0.0004 \quad (A) \tag{2.11b}$$

In order to apply to the PMSG equation the relations (2.11), they must be converted to the same $dq0$ referential. Again, tests were made in [7], which resulted in the following relations:

$$u_q = 1.5\sqrt{\frac{2}{3}}\,U \tag{2.12a}$$

$$i_q = 1.5\sqrt{\frac{2}{3}}\,I \tag{2.12b}$$

being R_a the sum of the PMSG coil resistances, R_c the circuit imposed resistance (and the controlled variable), and $R = R_a + R_c$, the modified state space of the PMSG is given by:

$$\frac{di_q}{dt} = -\frac{R_a + R_c}{L} 1.2247(0.0089\,\omega + 0.0004) - n_p\,\omega \frac{\lambda_0}{L} - n_p\,\omega\,i_d + \frac{1}{L} 1.2247(0.2841\,\omega + 0.2193) \tag{2.13a}$$

$$\frac{di_d}{dt} = n_p\,\omega\,i_q \tag{2.13b}$$

Drive Train

The drive train ensures the connection between the rotor and PMSG. Resorting to [32], the equation for the one mass drive train is given by:

$$J_t\,\dot{\omega} = T_a - T_{em} \tag{2.14}$$

where J_t is the moment of inertia for blades, hub and generator, T_a is the aerodynamic torque given by (2.7) and T_{em} is the electromagnetic torque given by (2.10).

2.1.2 Linear Model

A generalized dynamic linear model was obtained in [17] resorting to the Taylor series around a generic operating point. The linearisation of the aerodynamic torque is given by:

$$T_a(v,\omega) \approx \overline{T_a} + a\,\delta v + b\,\delta\omega \tag{2.15}$$

where $\delta v = v - \overline{v}$, $\delta\omega = \omega - \overline{\omega}$ and a and b are given by:

$$a = \left.\frac{\partial T_a}{\partial v}\right|_{opt} \qquad b = \left.\frac{\partial T_a}{\partial \omega}\right|_{opt} \tag{2.16}$$

where opt is the parameter values where the linearisation is being performed, namely wind speed an angular speed. Linearising (2.13a) and (2.13b) around a generic operating point, the following linearised equations are obtained:

$$\delta\dot{i_q} \approx c\,\delta R_c + d\,\delta\omega + g\,\delta i_d \tag{2.17}$$

$$\delta\dot{i_d} \approx j\,\delta\omega + k\,\delta i_q \tag{2.18}$$

where $\delta\dot{i_q} = \dot{i_q} - \dot{\overline{i_q}}$, $\delta\dot{i_d} = \dot{i_d} - \dot{\overline{i_d}}$, $\delta R_c = R_c - \overline{R_c}$, and c, d, g, j and k are given by:

$$c = \left.\frac{\partial\dot{i_q}}{\partial R_c}\right|_{opt} \tag{2.19}$$

$$d = \left.\frac{\partial\dot{i_q}}{\partial \omega}\right|_{opt} \tag{2.20}$$

$$g = \left.\frac{\partial\dot{i_q}}{\partial i_d}\right|_{opt} \tag{2.21}$$

$$j = \left.\frac{\partial\dot{i_d}}{\partial \omega}\right|_{opt} \tag{2.22}$$

$$k = \left.\frac{\partial\dot{i_d}}{\partial i_q}\right|_{opt} \tag{2.23}$$

$$\tag{2.24}$$

Linearising around an operating point, the electromagnetic torque expressed in (2.10) is given by:

$$T_{em} \approx \overline{T_{em}} + e\,\delta i_q \tag{2.25}$$

where $\delta i_q = i_q - \overline{i_q}$, and e is given by:

$$e = \left.\frac{\partial T_{em}}{\partial i_q}\right|_{opt} = 1.5\, n_p\, \lambda_0 \tag{2.26}$$

To obtain the final linear dynamic model it is important to merge the linearised quantities of interest. Merging (2.15), (2.25) and (2.14), a linear relation is achieved:

$$\delta\dot{\omega} \approx J_t^{-1}\left(\overline{T_a} + a\,\delta v + b\,\delta\omega - \overline{T_{em}} - e\,\delta i_q\right) \tag{2.27}$$

Applying Laplace transform to (2.27):

$$s\Delta\omega \approx J_t^{-1}\left(\overline{T_a} + a\,\Delta v + b\,\Delta\omega - \overline{T_{em}} - e\,\Delta i_q\right) \tag{2.28}$$

Considering $\overline{T_a} = \overline{T_{em}}$ the following simplification arises:

$$s\Delta\omega \approx J_t^{-1}\left(a\,\Delta v + b\,\Delta\omega - e\,\Delta i_q\right) \tag{2.29}$$

Rearranging (2.29), and introducing (2.17) and (2.18), the general third order transfer function is given by:

$$\Delta\omega(s) = \frac{a(s^2 - g\,k)}{J_t\,s^3 - b\,s^2 + (J_t\,k\,g)s + b\,k\,g + j\,g\,e}\Delta v(s) + \\ \frac{-e\,c\,s}{J_t\,s^3 - b\,s^2 + (J_t\,k\,g)s + b\,k\,g + j\,g\,e}\Delta\omega(s) \tag{2.30}$$

2.2 Darrieus VAWT Prototype

The wind power generator on which the present document is focused is a Darrieus vertical axis wind turbine (VAWT). The innovative blade profiles were designed and developed in [6] and have been studied in numerous publications. In this section, the prototype's technical characteristics will be presented and the different models developed in [7] will be analysed. Finally, some considerations will be made with regard to the optimal operating point.

2.2.1 Prototype Considerations

As stated in [4], for performance simulations when studying the blade's profiles, it was assumed that the turbine had $4.6\ \mathrm{m}$ of height and a blade radius of $2\ \mathrm{m}$. However, the prototype built has different dimensions. The main physical specifications are presented in table 2.1.

The PMSG present in the prototype was adapted from a SAV-15W produced by *SAIAM* a commercial version H-Darrieus VAWT. In A is included a brochure from this small wind turbine, that presents some technical specifications related to the PMSG. The number of poles (n_p), the stator resistance(R_a) and the inductance (L) were determined experimentally in [17]. These specifications are presented in Table

Table 2.1: Turbine's Specifications.

PARAMETERS	SYMBOL	VALUE
$N^{\text{o}}\ of\ Blades$	Z	5
$Rotor\ Height$ [mm]	H	480
$Rotor\ Radius$ [mm]	r	173
$Blade\ Body\ Height$ [mm]	-	360
$Blade\ Profile\ Chord$ [mm]	c	53
$Moment\ of\ Inertia$ [kgm^2]	J_t	0.1

2.2.

Table 2.2: PMSG Specifications.

PARAMETERS	SYMBOL	VALUE
$Generator\ Type$	-	$3-phase\ ACPMG$
$Number\ of\ Poles$	n_p	6
$Rated\ Voltage$ [V]	$-$	12
$Stator\ Resistance[\Omega]$	R_a	18.74
$Permanent\ Magnet\ Flux$ [$\mathrm{W}_{\mathrm{bturns}}$]	λ_0	0.272
$Inductance$ [mH]	L	24

This data was used to complete the model introduced in section 2.1, the different models one had available to develop the controllers are addressed in detail in the next section. To assess the veracity of the models considered, and to be able to have a supported critical view regarding the model's behaviour, it is important to observe some real data from the prototype. In Figure 2.1 is presented real data collected in [4].

The data presented was collected with the PMSG in open circuit, therefore it represents the higher $\frac{\omega_{[rad/s]}}{v_{[m/s]}}$ relation capable by the turbine in the present configuration. As this type of VAWT has a fixed pitch, it is expected that the rotor's angular speed behaviour is directly proportional to the incoming wind speed. The data can be roughly described by the relation (2.31) or (2.32):

$$\frac{\omega_{[RPS]}}{v_{m/s}} = 0.325 \tag{2.31}$$

$$\frac{\omega_{[rad/s]}}{v_{m/s}} = 2.04 \tag{2.32}$$

Taking into account the relation (2.32) as the maximum achievable by the prototype with this PMSG,

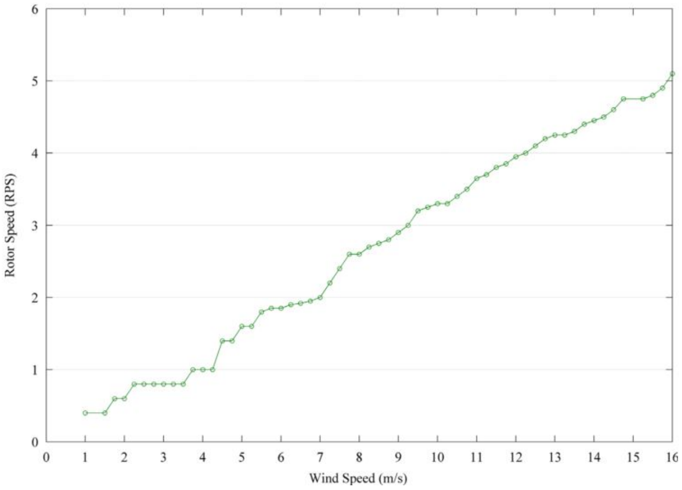

Figure 2.1: Real Prototype Data, Wind Speed vs Angular Speed.

one can calculate the corresponding maximum TSR, given by:

$$\lambda_{max} = 2.04 \cdot r \approx 0.353 \tag{2.33}$$

The $C_P(\lambda)$ function proposed for the turbine in [4] is shown in Figure 2.2.

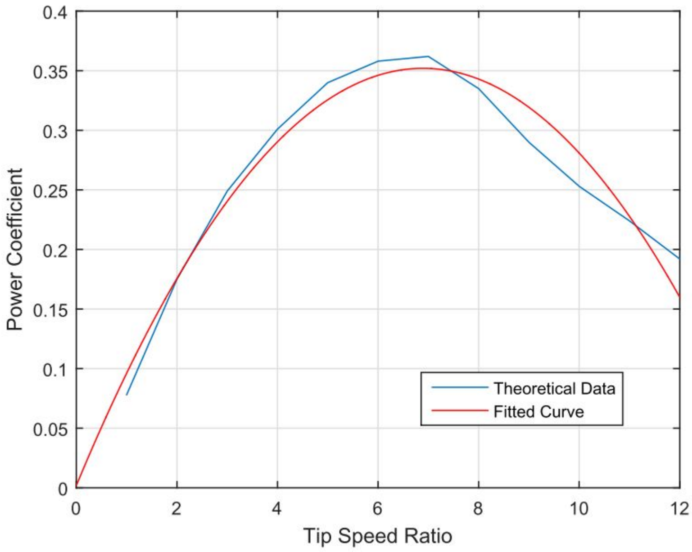

Figure 2.2: Power Coefficient (C_p) vs Tip Speed Ratio (λ) [4].

The fitted curve is given by:

$$C_P(\lambda) = -0.007365\,\lambda^2 + 0.1015\,\lambda + 0.002052 \tag{2.34}$$

It is important to notice that the simulation performed that originated the theoretical relationship presented in Figure 2.2 considers that the turbine has $4.6\,\mathrm{m}$ of height and $2\,\mathrm{m}$ of radius. Therefore, it is expected that the theoretical models built using (2.34) do not describe rigorously the prototype in hands. This said, instead of using as reference the TSR value used in [7] and [17], which is definitely impossible to reach, a plausible hypothetical value will be assumed as $\frac{2}{3}$ of the maximum TSR:

$$\lambda_{opt} = \frac{2}{3}\lambda_{max} \approx 0.2353 \tag{2.35}$$

This value will be used for simulation purposes in the remaining of this document.

Case Study

For the linear models, a theoretical case study was considered in [17]. This case study considers a wind speed of $6\,\mathrm{m/s}$ and, in order to have optimal conditions, according to equation (2.34), the rotor angular speed is set to $239.0658\,\mathrm{rad/s}$. In Table 2.3 the case study operating conditions from [17] are presented.

Table 2.3: Case Study Operating Conditions

PARAMETERS	SYMBOL	VALUE
$Nominal\ Wind\ Speed$ [m/s]	$\overline{v}$	6
$Nominal\ Angular\ Speed$ [rad/s]	$\overline{\omega}$	239
$Nominal\ Load\ Resistance$ [Ω]	$\overline{R_c}$	136.6
a	−	0.0138
b	−	-1.1507×10^{-4}
c	−	-35.478
d	−	-0.01909
e	−	2.448
g	−	-1.43×10^{3}
j	−	0.0674
k	−	1.43×10^{3}

2.2.2 Models Considered

Several models were developed in [7]. This section will focus in five of them which will be presented and analysed in order to select the more adequate model to develop the controllers. The five models considered are:

- Non-linear model;
- Third order linear model based in theoretical Case Study;
- Second order linear model based in theoretical Case Study;
- Single input single output identified model;
- Multiple input single output identified model.

Non-Linear Model

The non-linear model was developed in [17] resorting to the set of dynamic equations presented in section 2.1, combining (2.7), (2.10) and (2.14). This model makes use of (2.34) for the $C_P(\lambda)$ function. To compare the models available, all of them were tested in open-loop with a step input. The model's behaviour when subject to a wind step of $v = 10\,\mathrm{m/s}$ at $t = 0\,\mathrm{s}$ is presented in Figure 2.3 the circuit imposed resistance is kept at a high value of $R_c = 400\,\Omega$ to simulate the PMSG in open circuit.

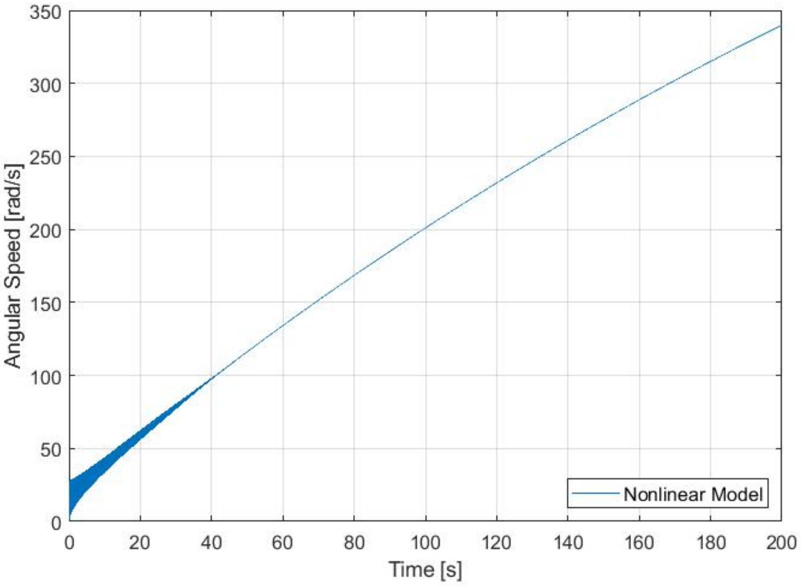

Figure 2.3: Non-Linear Open-Loop Step Response ($v = 10\,\mathrm{m/s}$, $R_c = 400\,\Omega$).

It is easily observed that the model does not represent the behaviour of the prototype as the Angular Speed do not stabilizes around $20\,\mathrm{rad/s}$ as it should, but instead keeps rising. This discrepancies are due to the error on the power coefficient function described in section 2.2.1 .

Third Order Model

The third order model presented in [7] is based on the linearised dynamic model described in (2.30) and the theoretical case study presented in Table 2.3. The model's transfer function is given by:

$$\Delta\omega(s) = \frac{0.1624\,s^2 + 3.32\times10^5}{s^3 + 0.001354\,s^2 + (2.045\times10^6)\,s - 7.488}\Delta v(s) + \frac{1022\,s}{s^3 + 0.001354\,s^2 + (2.045\times10^6)\,s - 7.488}\Delta\omega(s) \qquad (2.36)$$

This model was fed with a step input in the wind speed variation $\delta v = 4\,\mathrm{m/s}$ at $t = 20\,\mathrm{s}$ for a final value of $v = 10\,\mathrm{m/s}$. The load imposed resistance was kept at its nominal value with $\delta R_c = 0\,\Omega$ until $t = 100\,\mathrm{s}$, thereafter being changed for $\delta R_c = -40\,\Omega$ for a final value of load imposed resistance of $R_c = 96.6\,\Omega$. The simulation model's response is presented in Figure 2.4.

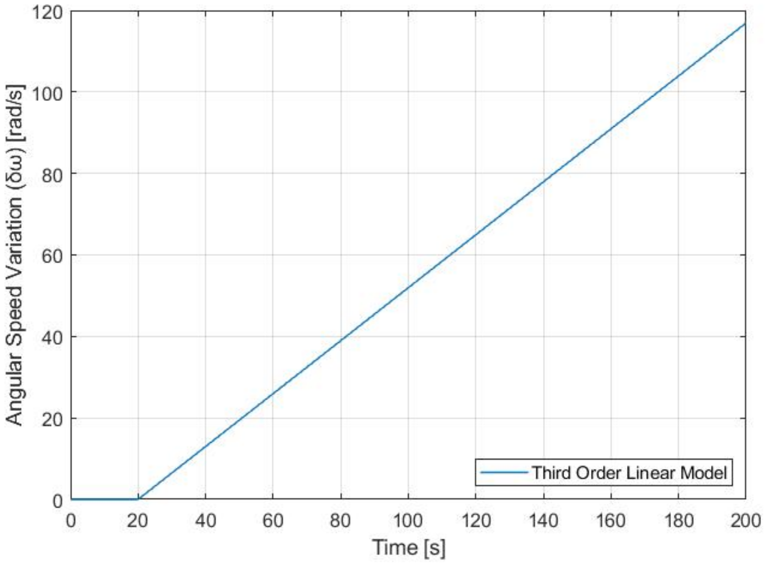

Figure 2.4: Third Order Model Open-Loop Step Response.

The response produced by the model is consistent with the case study, however it does not comply with the behaviour expected by the prototype, as a variation of $4\,\mathrm{m/s}$ in the wind input resulted in a exorbitant variance in angular speed, and the system not reacting to the load imposed resistance variation.

Second Order Model

This models was also developed in [7] and it consists of a simplified version of the third order model, excluding the dynamics associated with $\dot{\delta i_d}$. This second order model is given by:

$$\Delta\omega(s) = \frac{a\,s}{Jt\,s^2 - b\,s + e\,d}\,\Delta v(s) + \frac{-e\,c}{Jt\,s^2 - b\,s + e\,d}\,\Delta\omega(s) \tag{2.37}$$

When applying the case study coefficients from Table 2.3, the model assumes the form:

$$\Delta\omega(s) = \frac{0.1624\,s}{s^2 + 0.001354\,s - 0.3139}\,\Delta v(s) + \frac{1022}{s^2 + 0.001354\,s - 0.3139}\,\Delta\omega(s) \tag{2.38}$$

No simulation tests are presented for this model, as both transfer functions are unstable in open-loop, and instabilize for a step input.

SISO Third Order Identified Model

This model was obtained by single input single output identification methods in [7], and the two transfer functions were identified separately, therefore, as expected, the denominator of both transfer functions is not the same. Nonetheless, in [7] it is claimed that this model have fitted 99% of the $\frac{\Delta\omega(s)}{\Delta v(s)}$ testing data set, and 86% of the $\frac{\Delta\omega(s)}{\Delta R_c(s)}$.

The SISO model identified is given by:

$$\Delta\omega_{(s)} = \frac{0.2214\,s^2 + 0.00256\,s + 7.593\times10^{-5}}{s^3 + 0.1564\,s^2 + 0.001808\,s + 3.36\times10^{-5}}\Delta v_{(s)} + \frac{0.001159\,s + 1.5\times10^{-6}}{s^3 + 10.43\,s^2 + 2.25\,s + 7.5\times10^{-4}}\Delta Rc_{(s)} \tag{2.39}$$

The model was fed with a step input in the wind speed variation $\delta v = 10\,\mathrm{m/s}$ at $t = 20\,\mathrm{s}$. The load imposed resistance was kept at $\delta R_c = 150\,\Omega$ to simulate the PMSG in open circuit until $t = 100\,\mathrm{s}$, thereafter being changed for $\delta R_c = 5\Omega$. The simulation model's response is presented in Figure 2.5(a).

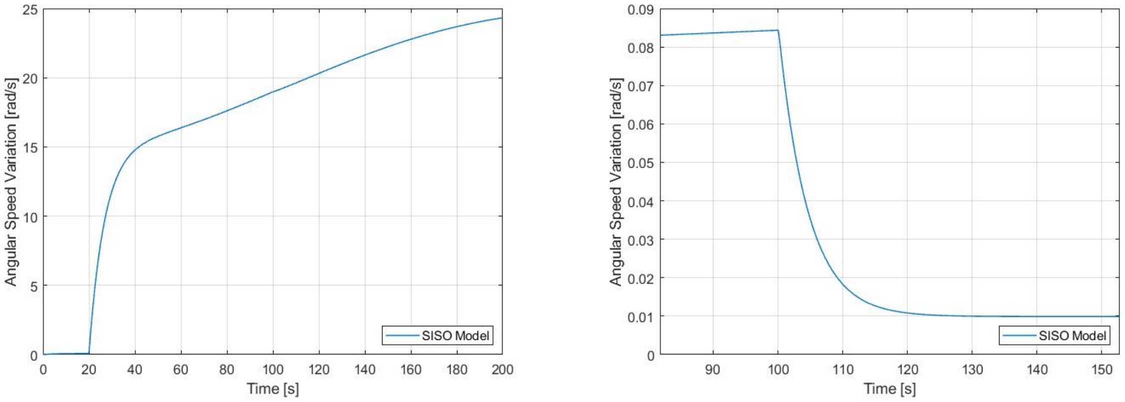

(a) Angular Speed Variation.

(b) ΔR_c influence in $\Delta\omega$.

Figure 2.5: SISO Identified Model Open-Loop Step Response.

Although the angular speed variation is within the order of magnitude the prototype should have with the PMSG in open-circuit, the influence from the load imposed resistance variation is almost null, a change in the R_c from 150Ω to 5Ω at $t = 100\,\mathrm{s}$ only results in an approximate $0.07\,\mathrm{rad/s}$ decrease in the angular speed as presented in Figure 2.5(b). Tests presented in the chapter 6 demonstrate that this value is almost 100 times smaller than it should be.

MISO Identified Model

The model with a higher fitting value presented in [7] was obtained resorting to multiple input single input identification methods with fixed rank ($n = 2$) and total parameter freedom. Fitting up to 85.26% of the test data set, the identified second order state space has as state vector $\mathbf{x} = [\delta\omega\ \delta i_q]^T$, as input $\mathbf{u} = \delta R_c$, and as disturbance $\mathbf{e} = \delta v$ and its given by:

$$\begin{cases} \dot{\mathbf{x}}(t) = A\,\mathbf{x}(t) + B\,\mathbf{u}(t) + E\,\mathbf{e}(t) \\ \mathbf{y} = C\,\mathbf{x}(t) + D\mathbf{u}(t) \end{cases} \tag{2.40}$$

where A, B, C, D and E are given by:

$$A = \begin{bmatrix} -1.32\times10^4 & -44.32 \\ -28.77 & -0.2376 \end{bmatrix} \qquad B = \begin{bmatrix} 952 \\ 3.718 \end{bmatrix} \qquad E = \begin{bmatrix} 7131 \\ -26.75 \end{bmatrix} \tag{2.41}$$

$$C = \begin{bmatrix} 1 & 0 \end{bmatrix} \qquad D = \begin{bmatrix} 0 & 0 \end{bmatrix} \tag{2.42}$$

As the quantity that has the most importance in our control problem is $\delta\omega$, and is of utmost importance to have the transfer functions to be able to develop the controllers, the conversion from state space to transfer function was made, and the transfer functions are given by:

$$\Delta\omega_{(s)} = \frac{7131\,s + 2879.9}{s^2 + 13200\,s + 1861}\Delta v_{(s)} + \frac{952\,s + 61.41}{s^2 + 13200\,s + 1861}\Delta Rc_{(s)} \tag{2.43}$$

The simulation test performed in the previous section was repeated, this time with the MISO identified model. The model was fed with a step input in the wind speed variation $\delta v = 4\,\mathrm{m/s}$ at $t = 20\,\mathrm{s}$. The load imposed resistance was kept at $\delta R_c = 0\,\Omega$ until $t = 100\,\mathrm{s}$, thereafter being changed for $\delta R_c = -100\Omega$. This model is a linear model around the working point $\overline{v} = 6\,\mathrm{m/s}$ and $\overline{R_c} = 136.6\,\Omega$. The model's response is presented in Figure 2.6.

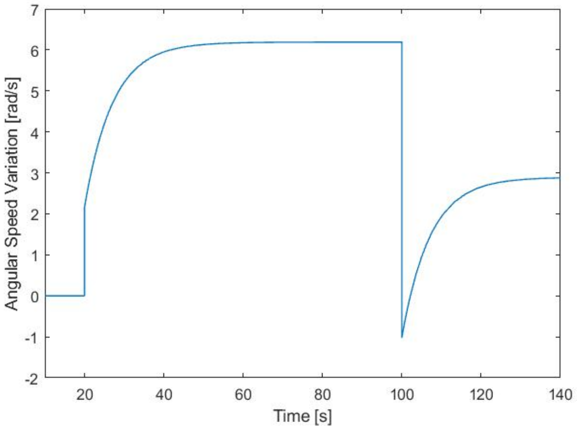

Figure 2.6: Multiple Input Single Output Response.

The model's response, in line with what was said in [7] and in [17], is the most satisfactory of all the models considered. However, the reaction to the R_c input is not exactly the one observed in the prototype, the general response is the expected (maintaining the angular velocity when in steady state, and decreasing it when the imposed load resistance diminishes from $136.6\,\Omega$ to $36.6\,\Omega$.

The wind speed variation effect in the angular speed has much faster dynamics than the real prototype, resulting in an instant increase of $2\,\mathrm{rad/s}$ at $20\,\mathrm{s}$, a growth that should be gradual. Nonetheless, this is the model that has a greater fit to the real data from the prototype, therefore, it will be used to synthesize the controllers and to simulate the prototype's behaviour.

2.2.3 Turbine Control Strategies

The power curve of a turbine is very important when defining the control strategy to be used and developing the controller to be implemented [33]. A typical wind turbine power curve is presented in Figure 2.7.

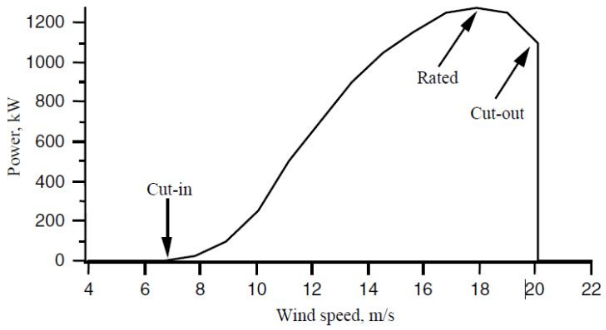

Figure 2.7: Typical Wind Turbine Power Curve [33].

From the power curve one can observe the different regimes of a wind turbine, delimited by different wind speeds, v_{cut-in}, v_{rated} and $v_{cut-out}$. The operating regimes of a wind turbine are:

- $v \leq v_{cut-in}$: The turbine is stopped as it only begins delivering power at v_{cut-in} wind speed although still far from its optimum performance;
- $v_{cut-in} \leq v \leq v_{rated}$: Regime at which the turbine is delivering power, but not the rated power it was designed for, the controller's objective in this section is to maintain th power coefficient (C_p) at its maximum, extracting as much energy as possible;
- $v_{rated} \leq v \leq v_{cut-out}$: At this point the turbine is delivering the rated power it was built for, the mode of operation is now changed to limit the power output, limiting the rotor speed and efficiency, in order to deliver a constant and stable rated power output;
- $v_{cut-out} \leq v$: The wind speed until which the turbine can operate in safety conditions has been reached, from this point on, the turbine is shut down to prevent structural damage.

As stated, for each working regime there is a different control objective, in Figure 2.8 the typical control strategies for fixed or variable speed, and stall or pitch regulated turbines are presented. To be noted, are wind turbines that are both stall and pitch regulated, therefore having more options to achieve its objective.

The present work focus on developing a controller for the regime $v_{cut-in} \leq v \leq v_{rated}$ and the prototype in hands is a variable speed, stall regulated, consequently leading to a *Generator torque control for* $C_{p,max}$.

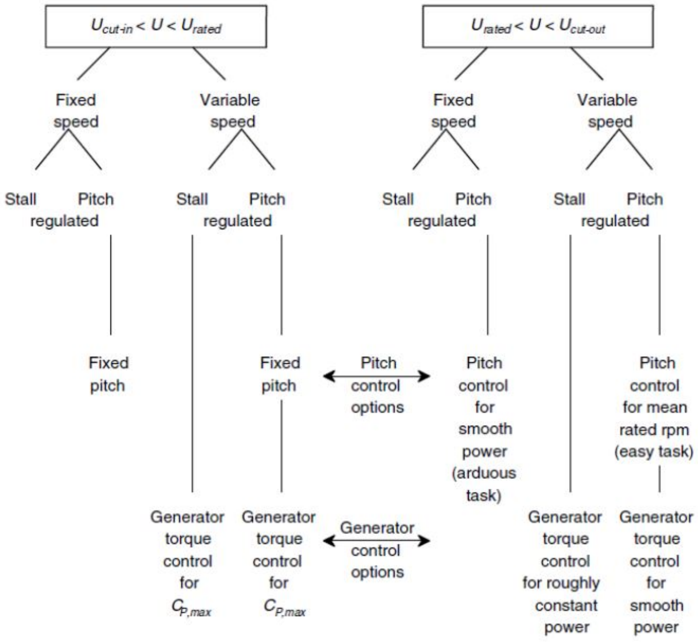

Figure 2.8: Overview of Typical Control Strategies [33].

2.3 Wind Characteristics

The wind is formed due to the uneven heating of Earth's surface by solar radiation. Differences in pressure across the globe impel air masses to dislocate originating this phenomenon. The wind velocity and direction can vary considerably with time, presenting a stochastic behaviour, making the wind an intermittent and unpredictable variable.

The wind phenomenon is frequently studied as having a vertical distribution described by a logarithmic profile. The direct interaction between Earth's surface and the atmosphere generates a vertical gradient in the wind flow, which is indicative of the wind speed variation relative to the height above the surface. The wind profile presents then a lower velocity at ground level, and growing as the distance to the surface increases. This gradient is also increased due to the presence of obstacles to the wind stream at ground level such as trees, buildings, hills or other relevant formations.

In cases such as the present one, that the intention is to install wind turbines in urban areas, the study of the wind behaviour around buildings and other man made formations assumes a role of extreme importance. The accelerations and decelerations caused by the altered shape of wind streamlines can be either useful or unprofitable depending on where the turbine is located [9].

2.3.1 Wind Modelling

According to [30] this variation can be described in the frequency domain as a sum of harmonic components, being the higher frequencies related to atmospheric turbulence. As it is impossible to avoid the turbulence present in the wind, the solution is to consider the atmospheric turbulence as an element in the development of wind powered systems. The model chosen to simulate this turbulence present in the wind is given by:

$$v = v_0 \left[1 + \sum_k A_k \, \sin(\omega_k \, t) \right] \tag{2.44}$$

being k an index associated with the mechanical oscillation excited during the turbines rotation, A_k the amplitude of the k oscillation, and ω_k the frequency of the same oscillation. The mechanical oscillations are modelled by a frequency range between 0.1 and $10\,Hz$, in Table 2.4 are presented the values used for the turbulent wind modelling [30].

Table 2.4: Mechanical Oscillations.

Source	k	A_k	ω_k
$Assimetry$	1	0.01	ω_k
$TowerShadow$	2	0.08	$3\,\omega_k$
$Blades$	3	0.15	$9\,\pi$

2.4 CRONE Control System Design Methodology

The CRONE (French acronym for *Commande Robuste d'Ordre Non Entier*) CSD theory is based on the complex non integer derivation. It is a frequency domain approach that has been developed since the $1980s$. Three CRONE CSD methods have been developed sequentially, extending the field of application of this control system. In all three methods, the controller is designed resorting to fractional order integro-diferentiation, which is ultimately approximated to integer order integro-diferentiation to allow its application in the real model.

The great advantage of this control strategy over its competitors, is the ability to take in account plant uncertainties with no distinction of their nature, whether they are parametric (structured) or unstructured. Using frequency uncertainty domains, these uncertainties (or perturbations) are considered in a fully-structured form, avoiding overestimation, leading to controllers that are less conservative and therefore with higher performance. The fractional order, which is either real in the 1st and 2nd generations or complex in 3rd generation, allows parametrization of the open-loop transfer function using a small number of parameters streamlining the search for the optimal controller [34].

First Generation CRONE

The 1st generation CRONE control takes into account only gain-like uncertainties. It is based on achieving a constant phase of the controller around open-loop unit gain frequency ω_{cg} (Figure 2.9), and through this avoiding phase variations within a frequency range $[\omega_A;\omega_B]$, with $\omega_A < \omega_{cg} < \omega_B$. This CRONE controller is defined by a transmittance of the form:

$$C(s) = C_0 \left(\frac{1+\frac{s}{\omega_l}}{1+\frac{s}{\omega_h}} \right)^n \tag{2.45}$$

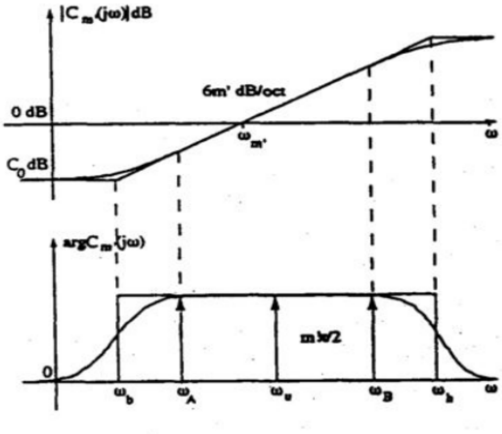

Figure 2.9: Bode Diagram of Ideal 1st gen. CRONE Controller [23].

Second Generation CRONE

The 2nd generation CRONE control cancels directly the variations of the phase margin at the time of the re-parametrization of the plant. The robustness of the control is illustrated for gain-like uncertainties by a vertical sliding of the template (Figure 2.10), that the open loop Nichols locus forms for the nominal parametric state ($G_0(s)$) around open-loop unit gain frequency ω_{cg}. This allows not only a constant phase margin in the interval $[\omega_A; \omega_B]$, but also a constant first overshoot and damping ratio, by ensuring the tangency from the template to both the *overshoot contour* (D_1') and the *damping contour*(ξ) between $[\omega_A; \omega_B]$ [24].

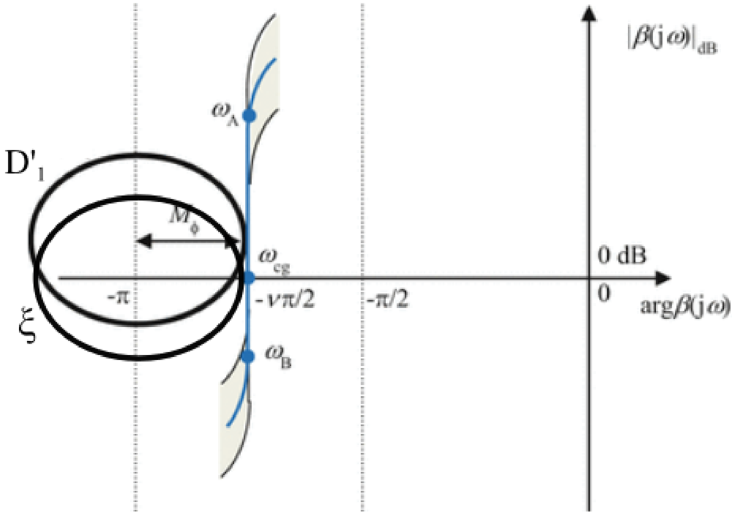

Figure 2.10: Vertical Template of the 2nd gen. CRONE [34].

In this controller, one does not define a controller formula; instead, the vertical template ($\beta(s)$) is defined and it is given by:

$$\beta(s) = \left(\frac{\omega_u}{s}\right)^n \tag{2.46}$$

And after having the vertical template (Figure 2.10), the controller can be computed by the ratio between vertical template and nominal plant transfer function:

$$C(s) = \frac{\beta(s)}{G_0(s)} \tag{2.47}$$

Third Generation CRONE

The 3rd generation CRONE controller is capable of handling not only gain-like uncertainties, but also uncertainties in the plant's phase. This characteristic makes it the most powerful of the three CRONE methods [34]. The main objective of this type of control is to ensure that the closed-loop gain or damping coefficient, or both, will never get beyond a certain value, even if some plant's parameter vary within a known range. Both these objectives correspond to prevent the open-loop Nichols plot from approaching zones where the closed-loop gain is high and damping coefficient is low.

In third generation CRONE the Nichols locus is still defined as a straight-line segment around frequency ω_{cg} for the nominal parametric state of the plant, but not necessarily vertical: it can assume any direction. Whereas the vertical template is based on the real fractional-order transfer function (2.46), the generalized template is based on the real part of the fractional complex integration, when $n = a + i\,b \in C_i$. From [25], the open loop transfer function is given by:

$$\beta(s) = \left(\cosh\left(b\frac{\pi}{2}\right)\right)^{\mathrm{sign(b)}} \left(\frac{\omega_{cg}}{s}\right)^{a} \left(\Re_{/\mathrm{i}}\left(\frac{\omega_{cg}}{s}\right)^{\mathrm{ib}}\right)^{-\mathrm{sign(b)}} \tag{2.48}$$

Expanding (2.48) provides:

$$\beta(s) = \left(\cosh\left(b\frac{\pi}{2}\right)\right)^{\mathrm{sign(b)}} \left(\frac{\omega_{cg}}{s}\right)^{a} \left(\cos\left(b\,\ln\left(\frac{s}{\omega_{cg}}\right)\right)\right)^{-\mathrm{sign(b)}} \tag{2.49}$$

From the derivatives of the $\beta(\mathrm{j})$ magnitude and phase at frequency ω_{cg}, it can be proven that the angle of the generalized template to the vertical, can be expressed as a function of a and b [34] (Figure 2.11(a)). The real part a determines the phase location of the generalized template at frequency ω_{cg}, that is $-a\frac{\pi}{2}$, and the imaginary part b determines its angle to the vertical.

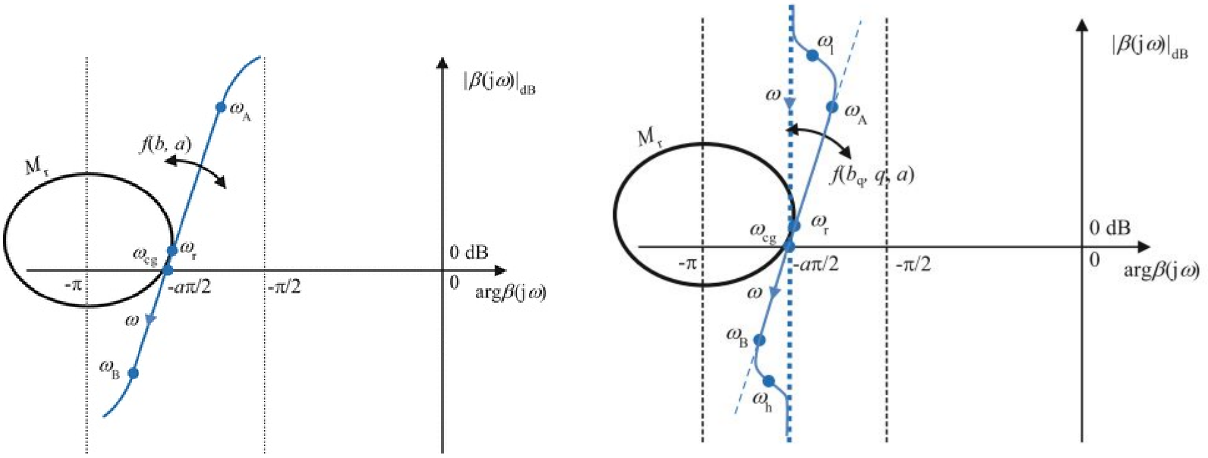

(a) Generalized Template. (b) Generalized Template Including the Band-Limited Integrator.

Figure 2.11: General Template Representation [34].

To ensure stability of the closed-loop system, the imaginary part of the integrator is band-limited, thus, the definition (2.49) of $\beta(s)$ can be replaced for:

$$\beta(s) = K\left(\frac{\omega_{cg}}{s}\right)^{a} \left(\Re_{/\mathrm{i}}\left(\alpha_0 \frac{1+\frac{s}{\omega_h}}{1+\frac{s}{\omega_l}}\right)^{\mathrm{ib}}\right)^{-\mathrm{sign(b)}} \tag{2.50}$$

where K ensures that $|\beta(\mathrm{j}\,\omega_{\mathrm{cg}})| = 1$ and $\alpha_0 = \frac{\omega_h}{\omega_l}\sqrt{\frac{\omega_{cg}^2+\omega_l^2}{\omega_{cg}^2+\omega_h^2}}$. Figure 2.11(b) shows how the band-limitation modifies the Nichols plot of $\beta(s)$(Figure 2.11(b)).

There are times in which the open-loop shaping parameters present in (2.50) are not enough to lead to a satisfactory performance. A generalization was developed in [35], that consists in replacing the generalized template by a set of similar templates called multi-templates, providing a curvilinear template that increases the loop-shaping feature.

The multi-template is the product of band-limited transfer functions of type (2.50). The corresponding open-loop transfer function is given by:

$$\beta_m(s) = C_m \prod_{k=-N^-}^{N^+} \beta_{mk}(s) \tag{2.51}$$

where C_m ensures that $|\beta_{\mathrm{j}\omega_{\mathrm{cg}}}| = 1$, and $\beta_{mk}(s)$, α_0 and α_k are given by:

$$\beta_{mk}(s) = \left(\frac{1+\frac{s}{\omega_{k+1}}}{1+\frac{s}{\omega_k}}\right)^{a_k} \left(\Re_{/\mathrm{i}}\left(\left(\alpha_k \frac{1+\frac{s}{\omega_{k+1}}}{1+\frac{s}{\omega_k}}\right)^{\mathrm{ib_k}}\right)\right)^{-\mathrm{sign(b_k)}} \tag{2.52}$$

$$\alpha_0 = \left(\frac{1+\left(\frac{\omega_{cg}}{\omega_0}\right)^2}{1+\left(\frac{\omega_{cg}}{\omega_1}\right)^2}\right)^{1/2} \tag{2.53}$$

$$\alpha_k = \left(\frac{\omega_{k+1}}{\omega_k}\right)^{1/2} \qquad for\ k \neq 0 \tag{2.54}$$

In Figure 2.12 the effect of the multi-template solution in the Nichols locus is presented.

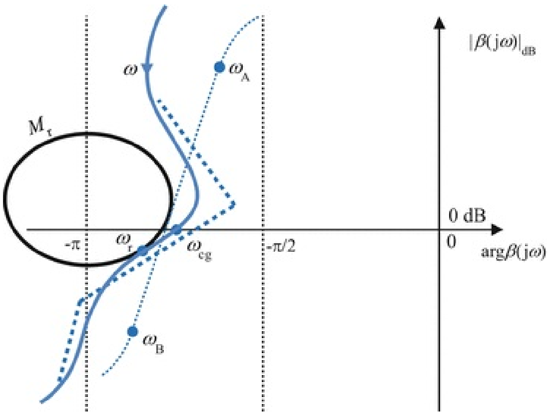

Figure 2.12: Rectilinear Template ($\cdots$); Multi-Template ($---$); Curvilinear Template ($-$); from [34]

Optimal Template

The desired nominal resonant peak M_{rd} can be set for the nominal parametric state of the plant in order to ensure nominal performance. However, when considering the uncertainty of the plant, one has to account for the variations such uncertainties will cause in the M_r, and minimize the influence of the plants uncertainties to ensure stability.

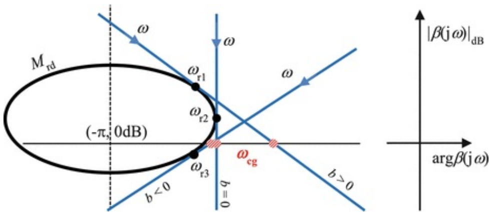

Figure 2.13: Three Generalized Templates that Tangent a Given M-contour, from [34]

For each frequency ω_i an uncertainty domain can be defined as the smallest convex-hull that includes all the possible frequency responses $\beta(\mathrm{j}\omega_\mathrm{i})$ of the perturbed open-loop transfer function.

There is an indefinite number of generalized templates tangent to the desired M-contour for the nominal parametric state of the plant (Figure 2.13), from these, the Optimal Template (Figure 2.14) is the one that minimizes the M_r variations, that is, the template that minimizes the overlapping of the uncertainty domains (grey area) with M-contours higher than M_{rd}.

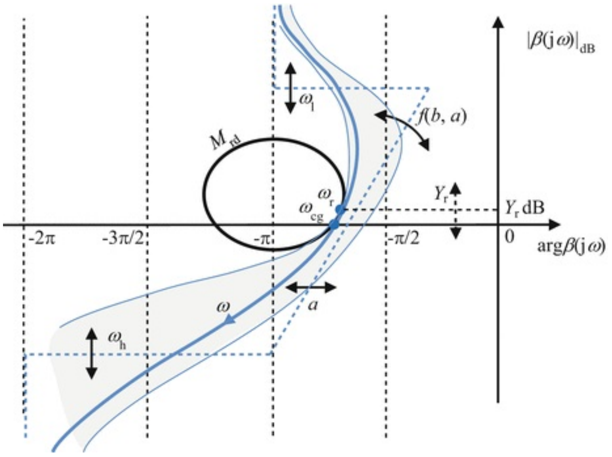

Figure 2.14: Optimal Template, from [34]

The optimal template is achieved resorting to a robustness-oriented cost function, that minimizes this overlapping, that function is given by:

$$J = \sup_{\omega, G} |T(\mathrm{j}\omega)| - \mathrm{M_{rd}} \tag{2.55}$$

Minimizing this cost function allows the optimal template to position the uncertainty domains so that they overlap the low stability margin areas of the Nichols chart as little as possible. The cost function is minimized subject to 5 frequency domain constraints. These constraints are given by:

$$\inf_{G} |T(\mathrm{j}\omega)| \geq T_l(\omega), \tag{2.56}$$

$$\sup_{G} |T(\mathrm{j}\omega)| \leq T_u(\omega), \tag{2.57}$$

$$\sup_{G} |S(\mathrm{j}\omega)| \leq S_u(\omega), \tag{2.58}$$

$$\sup_{G} |CS(\mathrm{j}\omega)| \leq CS_u(\omega), \tag{2.59}$$

$$\sup_{G} |SG(\mathrm{j}\omega)| \leq SG_u(\omega), \tag{2.60}$$

$$\tag{2.61}$$

where the complementary sensitivity function $T(\mathrm{j}\omega)$, the output sensitivity function $S(\mathrm{j}\omega)$, the control sensitivity function $CS(\mathrm{j}\omega)$ and the input sensitivity function $SG(\mathrm{j}\omega)$, are given by:

$$T(s) = \frac{\beta(s)}{1+\beta(s)} \tag{2.62}$$

$$S(s) = \frac{1}{1+\beta(s)} \tag{2.63}$$

$$CS(s) = \frac{C(s)}{1+\beta(s)} \tag{2.64}$$

$$SG(s) = \frac{G(s)}{1+\beta(s)} \tag{2.65}$$

Resorting to the CRONE Control Design Module for Matlab, these principles will be applied in the development of a third generation CRONE controller for the plant.

Chapter 3

Controller Development

3.1 Model Analysis

As seen before, in this system there are two inputs and one output (Figure 3.1(a)), as only the PMSG resistance (Rc) is controllable, the contribution from the wind velocity (v) to the output is treated as a disturbance present in the system that one can not predict (Figure 3.1(b)).

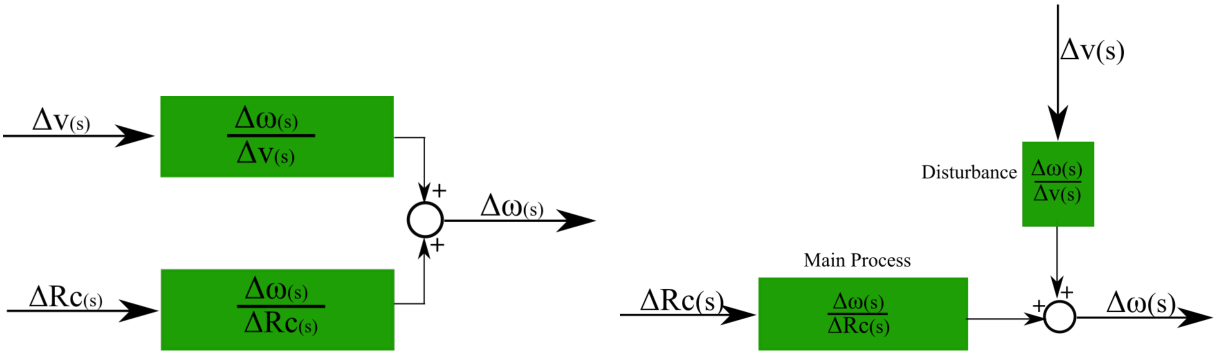

(a) 2 Inputs and 1 Output.

(b) 1 Input, 1 Disturbance and 1 Output.

Figure 3.1: Turbine Characteristics.

With this in mind, only the transfer function of the main process $\left(\frac{\Delta\omega(s)}{\Delta Rc(s)}\right)$ will be analysed for the controller synthesis. This transfer function is given by:

$$\frac{\Delta\omega(s)}{\Delta Rc(s)} = \frac{952\,s + 61.41}{s^2 + 13200\,s + 1861} = \frac{952(s + 0.645)}{(s + 13200)(s + 0.141)} \tag{3.1}$$

For a better understanding of the system's characteristics a root locus and bode diagram are shown in Figure 3.2.

The system has one real zero at $[-0.0645]$, two real poles at $[-13200; -0.141]$ and a static gain of 0.033. It is stable in closed loop for all values of $K \geq 0$. In the bode diagram one can see that the system has infinite gain and phase margins as it never crosses neither the $0\,dB$ gain line or the 180^o phase line.

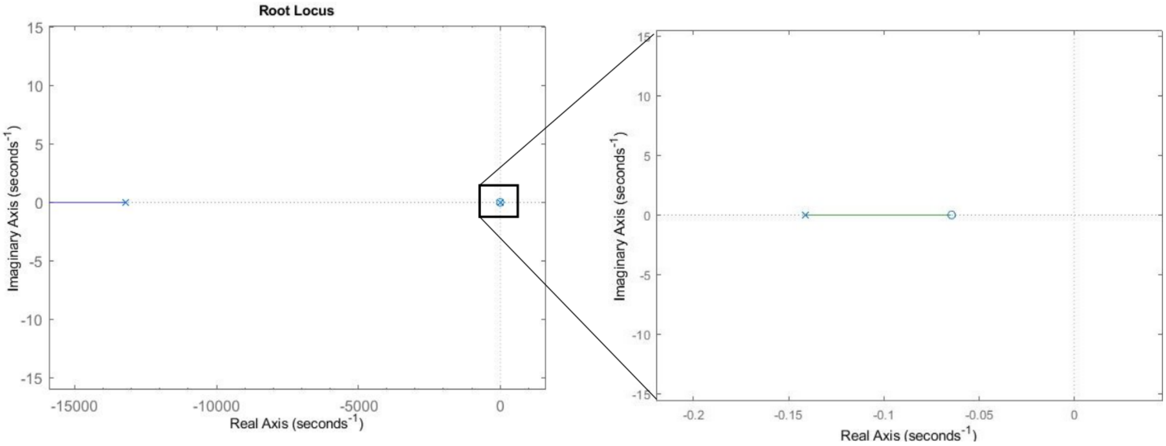

(a) Root Locus.

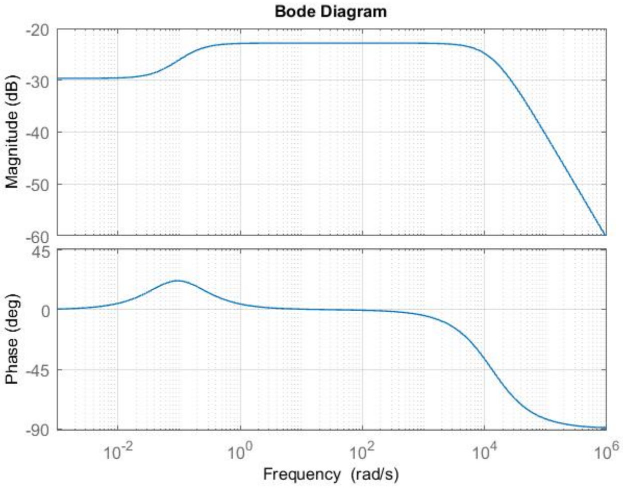

(b) Bode Diagram.

Figure 3.2: System's Characteristics.

As it has not been possible to acquire data from the real turbine at the time the controller was developed, the uncertainty present in the model was assumed to be of $\pm 20\%$. Two types of uncertainties were studied. The first was to consider this uncertainty in the zeros and poles position. Although it seemed more correct do it this way, when computing the structured uncertainty domains in the Nichols locus (Figure 3.3(b)), one can see that they assume an unusual form and do not contemplate the variations around the plant's nominal state. Therefore, it was decided to contemplate the uncertainty in the transfer function's coefficients, as it produced uncertainty domains around the nominal state, and with a more usual form.

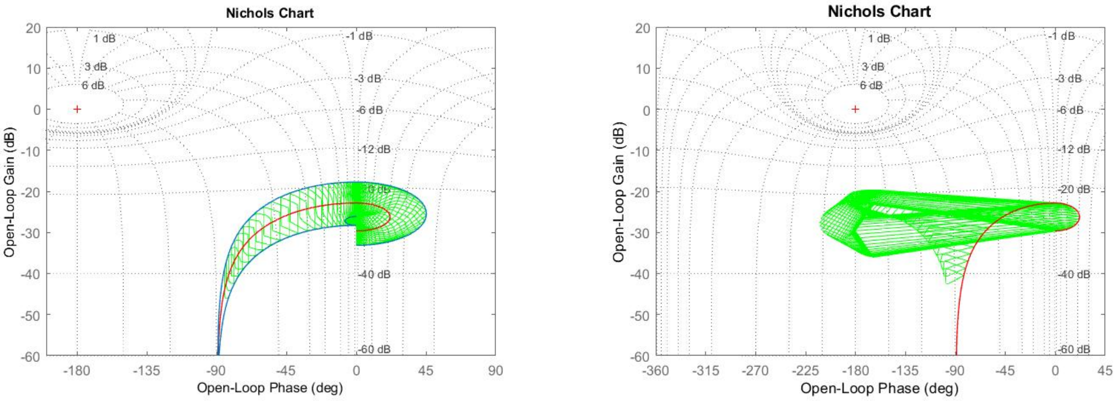

(a) $\pm 20\%$ Uncertainty in the Plant Coefficients.

(b) $\pm 20\%$ Uncertainty in Zeros and Poles Location.

Figure 3.3: Plant Nichols Locus With Uncertainty Domains.

The controller design will proceed only for the first case presented in Figure 3.3(a). In green are represented the uncertainty domains, in red the nominal plant, and in blue, the two extreme plants that mark the lower and upper limits of the plants uncertainties. These plants are useful to simulate the system's response in the extremes considered. The two extreme plants are given by:

$$\frac{\Delta\omega(s)}{\Delta Rc(s)} = \frac{1142\,s + 40.94}{s^2 + 8800\,s + 1861} = \frac{1142(s + 0.0358)}{(s + 8799.8)(s + 0.2115)} \tag{3.2}$$

$$\frac{\Delta\omega(s)}{\Delta Rc(s)} = \frac{761.6\,s + 92.11}{s^2 + 19800\,s + 1861} = \frac{761.6(s + 0.1209)}{(s + 198000)(s + 0.094)} \tag{3.3}$$

The difference in the bode plots between the three plants is presented in Figure 3.4.

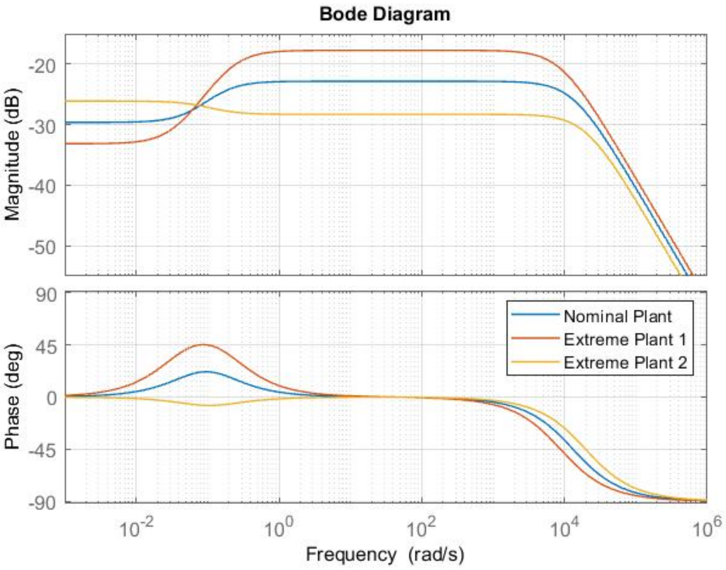

Figure 3.4: Nominal and Extreme Plants Bode Diagram.

From the bode diagram it is clear that the uncertainty considered in the plants is not only in the system's gain, which could be addressed resorting to second generation CRONE control, but also in the phase, reinforcing the need for a third generation CRONE controller.

To better understand the difference between the nominal plant and the two extreme plants, the open-loop simulation test performed in section 2.2.2 was repeated for the three models; the model's response is presented in Figure 3.5.

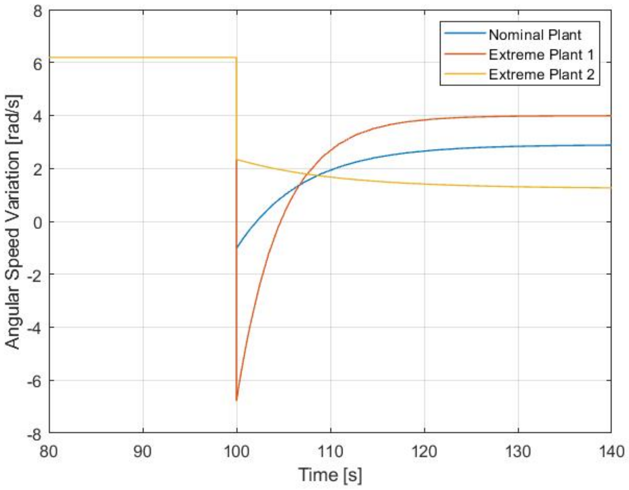

Figure 3.5: Nominal and Extreme Plants Open-Loop Step Response.

The step response presented in Figure 3.5 denotes the difference between the three plants, as expected, when introducing uncertainty in the system.

3.2 Control Objectives

The main objective of the control strategy is to maintain the turbine's efficiency at its maximum accounting wind speed variations. This translates into trying to maintain the Tip Speed Ratio (λ) in a value that maximizes the C_p, making use of the influence Rc has on ω, whatever the wind speed passing through the turbine. As stated in section 2.2.1, it will be assumed for simulation purposes that the λ_{opt} for which C_p is maximum is $\lambda = 0.2353$.

The specifications proposed in [17] for the system's closed-loop step response were:

- $Maximum\,Overshoot:\;M_p \leq 20\%$
- $Settling\,Time:\;t_s[2\%] \leq 10s$

3.3 Third Generation CRONE Control System Design

For the controller deign the *CRONE CSD Toolbox for Matlab* was used. This *Toolbox* has been developed by the CRONE Research Group at *Université de Bordeaux* since the late $80s$. The Toolbox allows to synthesize any CRONE controller, from first to third generation, by setting the specifications in the software and adjusting the different sensitivity functions that characterize the system.

The first step to synthesize the controller is to create a variable describing the plant with uncertainty, in Matlab environment. For this task, the the function *ltimodel2dataplant()* was used. This function is included in the *CRONE Toolbox*, and its inputs and outputs are described next.

$$[plantData] = ltimodel2plantfile(filename, G, pnom, pextr1, pextr2, \\ freq, Nfigure, nump, distribution, Nvertices, Dampinglimit); \quad (3.4)$$

- The output of this function is a *struct* which describes the perturbed plant fr the third generation CRONE CSD Toolbox.
- As inputs this function requires:
  - *filename*: is a string and defines where the result will be saved (*filenameCC3.mat*);
  - *G*: is a string which describes a plant with N uncertain parameters $p(i)$ with $i \leq 1 \leq N$. For example G can be defined by $2 * s * p(1)/(s^2 + p(2)/p(1) * s + 1)$;
  - *pnom*: is a vector (1byN) which defines the nominal value of parameters $p(i)$;
  - *pextr1*: is a vector (1byN) which defines the first extreme value of parameters $p(i)$;
  - *pextr2*: is a vector (1byN) which defines the second extreme value of parameters $p(i)$;
  - *freq(1,1:n)*: is the frequencies row vector where the frequency responses will be computed;
  - *Nfigure*: (default value 0) indicates the figure number for a plot of the result if different from 0;
  - *nump*: is a vector (1byN) which defines how many values of $p(i)$ are taken into account. The default value is *nump(i) = 5*;
  - *distribution*: is a cell which defines if the values of p(i) will be lin or log spaced. The default value is *distributioni='log'*.
  - *Nvertices* (default value 16) is the desired number of the uncertainty domain vertices;
  - *Dampinglimit*: (default value 0.1) defines the nominal zeros and poles that will be considered as underdamped

From this function, a file is created. In Figure 3.6 is presented the CRONE CSD Toolbox interface.

The next step is to select plant file created before, in the *plant* dropdown list. Next, the time response specifications are set, and the open loop parameters. The sensitivity functions are to be initialized in the next section, and can be observed in the dropdown list. The optimization of the fractional open-loop design is performed next, it is possible to manipulate the different variables that compose the generalized template. The strength of the Toolbox is shown when optimizing the generalized template, in such a way that the uncertainty domains overlap as little as possible the dangerous zones in the Nichols locus. The optimizing interface is presented in Figure 3.7.

By the end of the controller synthesis one has a fractional complex controller, impossible to implement, whereby, the *CRONE CSD Toolbox* has a section available that allows to manipulate a generic

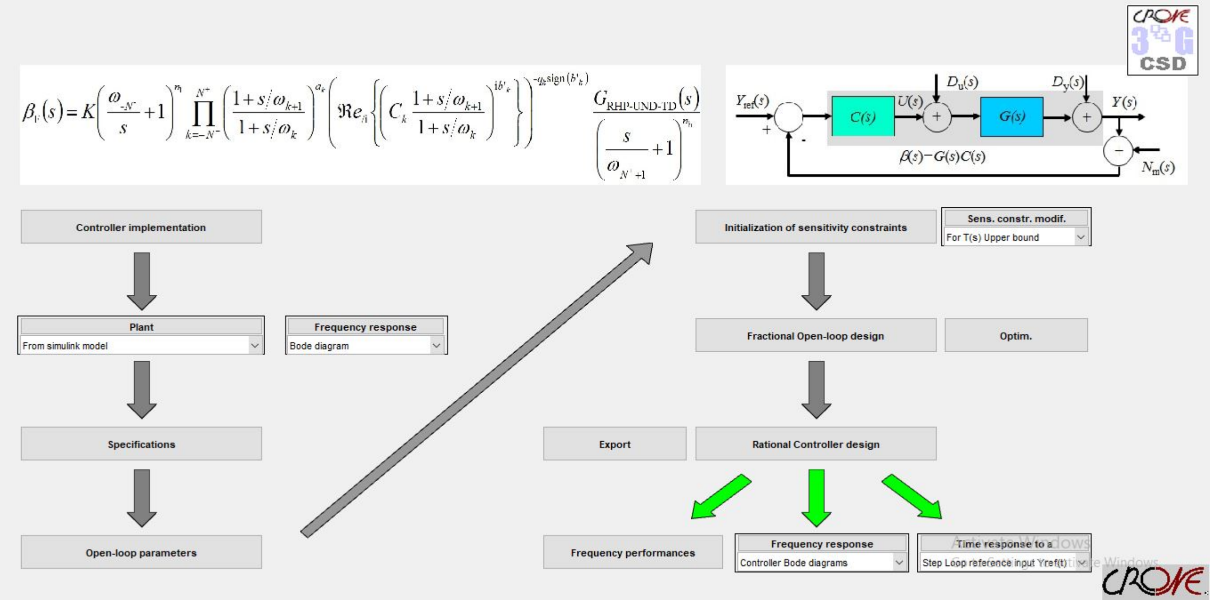

Plant: From simulink model

Frequency response: Bode diagram

Sens. constr. modif.: For T(s) Upper bound

Frequency response: Controller Bode diagrams

Time response to a: Step Loop reference input Yref(t)

Figure 3.6: General Layout CRONE Toolbox

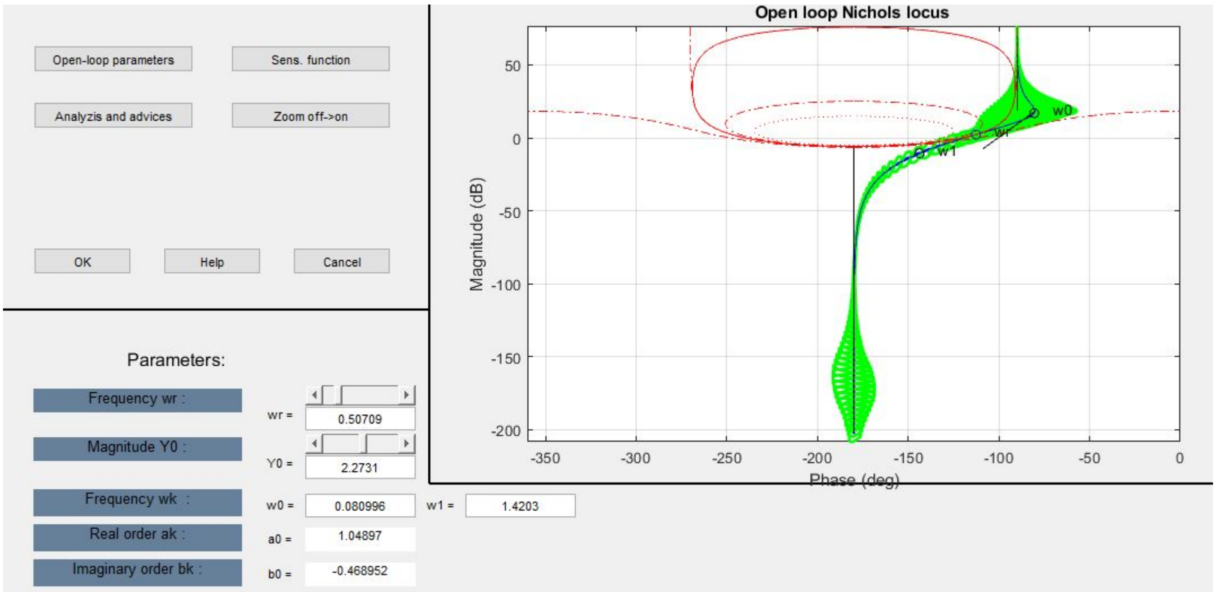

wr = 0.50709

Y0 = 2.2731

w0 = 0.080996

w1 = 1.4203

a0 = 1.04897

b0 = -0.468952

Figure 3.7: Open-loop Optimizer Interface in CRONE Toolbox

rational integer bode plot to approximate the fractional complex controller. In Figure **??** is shown this interface.

After several modifications of the parameters and sensitivity functions, the best controller synthesized is presented next.

$$C(s) = \frac{-23.524}{s+3.9295} + \frac{-9.0679}{s+0.34063} + \frac{32.5992}{s} \tag{3.5}$$

The bode diagrams from both fractional and rational controllers are presented in Figure 3.9. The difference between them is less than $0.5dB$ in magnitude, and less than 5^o in phase, concluding that the approximation is almost perfect.

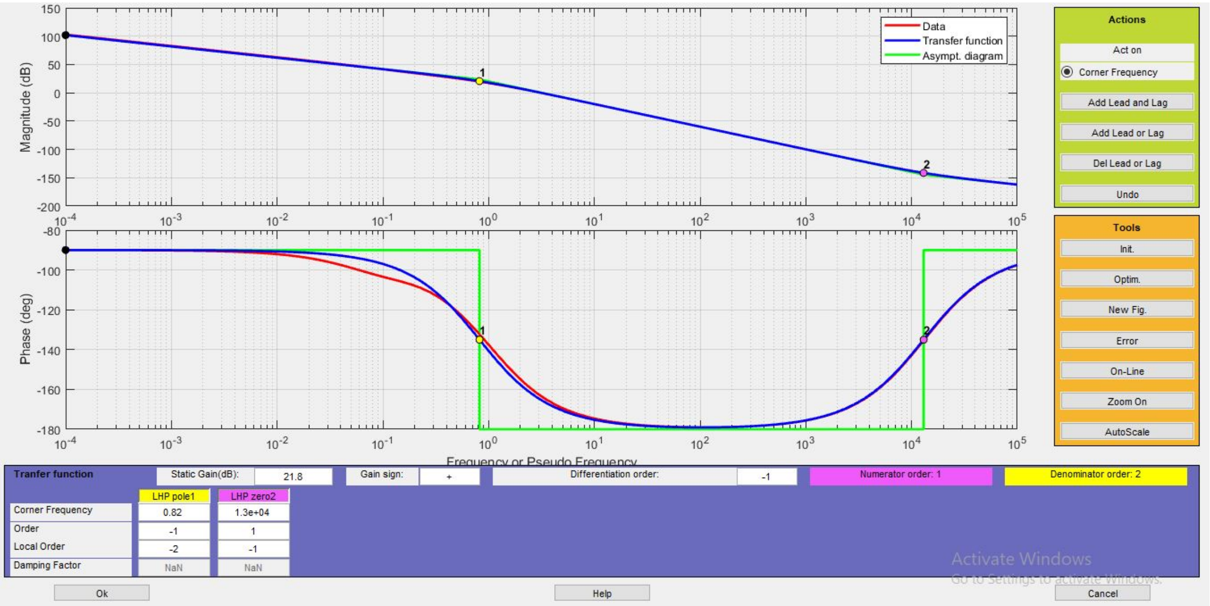

● Corner Frequency

Tranfer function

Static Gain(dB): 21.8

Gain sign: +

Differentiation order: -1

Numerator order: 1

Denominator order: 2

	LHP pole1	LHP zero2
Corner Frequency	0.82	1.3e+04
Order	-1	1
Local Order	-2	-1
Damping Factor	NaN	NaN

Figure 3.8: Rational Controller Design Interface in CRONE Toolbox

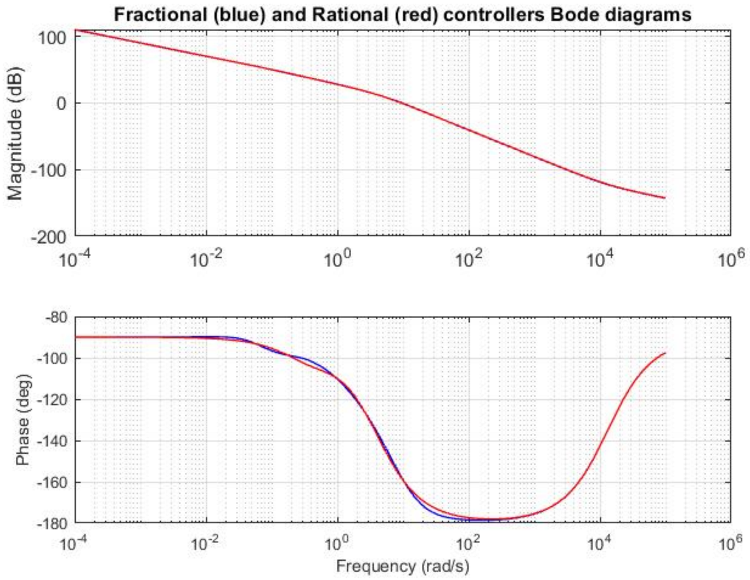

Figure 3.9: Fractional and Rational Controller Bode Diagrams.

The Nichols locus obtained after applying the fractional and the rational controllers are shown in Figure 3.10.

As expected, after applying the controller the Nichols locus becomes tangent to the desired M-contour, defining the resonant peak. And the uncertainty domains were arranged in such a way that the overlapping is reduced to a minimum.

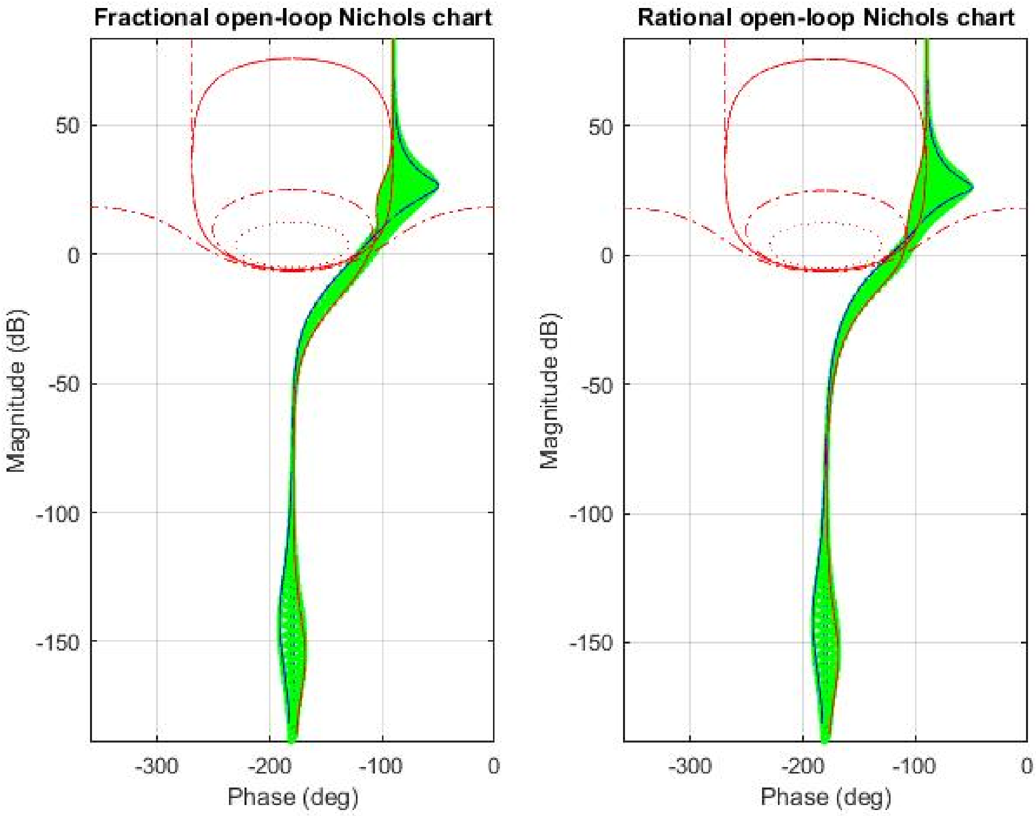

Figure 3.10: Fractional and Rational Open-Loop Nichols Locus.

Chapter 4

Simulation Results & Controller Performance

Directly from the *Toolbox* is built a graph (Figure 4.1) of the system's closed-loop response when a unit step is used as $\Delta\omega_{ref}(s)$ input, as well as a graph showing the respective control effort ΔRc. Both graphs can be used for a preliminary analysis of the controller performance.

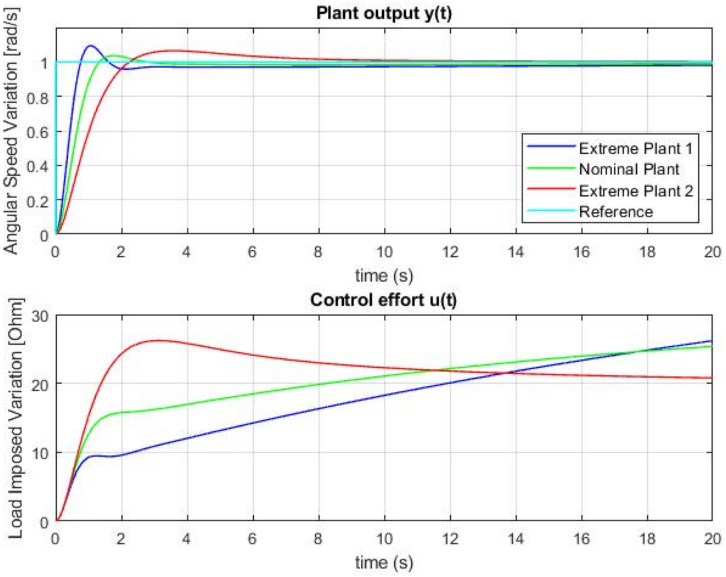

Figure 4.1: Controlled Closed-Loop Step Response - CRONE Toolbox

From the closed-loop response depicted above, one can observe that the system fulfils the specifications for all three plants. The control effort does not surpass the value of $\Delta Rc = 30\,\Omega$ which, as the model is linearised around $R_c = 136.6\,\Omega$, corresponds to $R_c = 166.6\,\Omega$.

Using *MATLAB*, more specifically *Simulink*, the loop was closed (Figure 4.2). In the block [*TSR* - $\Delta\omega_{ref}(s)$], is being computed the $\Delta\omega_{ref}(s)$ that ensures that the *TSR* is at the optimum value ($TSR = 0.2353$). The value obtained for $\Delta\omega_{ref}(s)$ is then compared to the actual $\Delta\omega(s)$ and the error between the two values is fed to the controller.

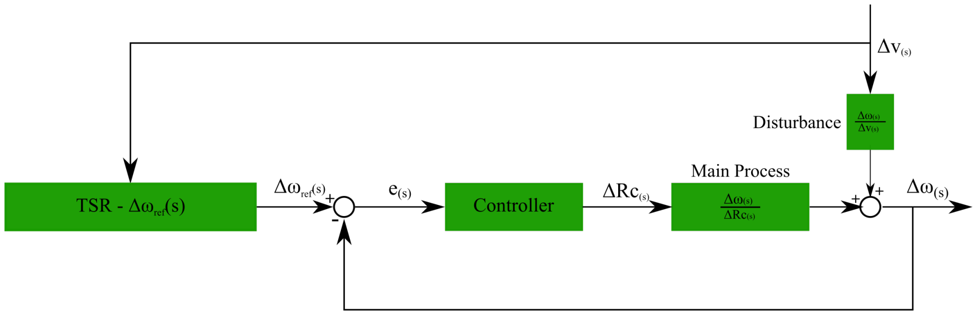

Figure 4.2: Closed-Loop Block Diagram.

4.1 Continuous Time Simulation

4.1.1 Without Turbulence

The controller was firstly tested using a step as wind perturbation, neglecting the turbulence present in the wind, to assess the controlled closed-loop system's behaviour and the uncontrolled responses, both in open-loop and closed-loop. In nature, the wind does not have an abrupt (*step-like*) behaviour, the variations should be smoother. However, it is valid to admit that, if the system behaves accordingly with a step input disturbance, in the presence of smoother disturbances its performance should be of higher quality.

For this test, the wind is kept at its nominal value, assumed to be $v = 6\,\mathrm{m/s}$, and at $t = 30s$ the disturbance is simulated as a step $\Delta v = 4\,\mathrm{m/s}$. For $t \geq 10s$ the wind velocity is kept at its final value $v = 10\,\mathrm{m/s}$.

Firstly, for comparison purposes, this test was performed in open-loop, and in closed-loop without controller ($C = 1$), for the nominal plant and both extreme plants. The results are presented in Figure 4.3.

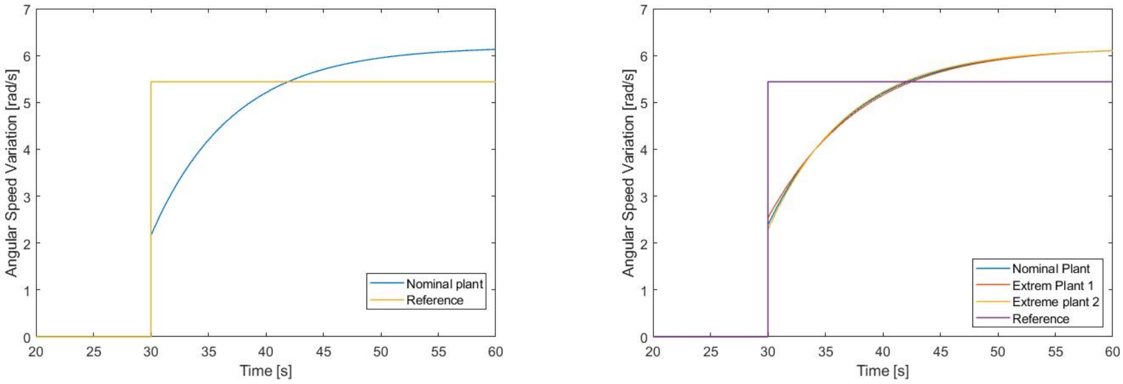

(a) Open-loop Response.

(b) Closed-loop Response ($C = 1$).

Figure 4.3: Uncontrolled Responses - Step Input.

Both responses are very similar, as the main contribution for the step response is given by the wind. In the open-loop step response (Figure 4.3(a)), the step responses from the three different plants are equal. This is due to the fact that, the uncertainty is only considered in the transfer function $\frac{\Delta\omega(s)}{\Delta Rc(s)}$.

Therefore, as in open-loop the ΔRc is kept constant, the uncertainty domains have no influence in the response. In closed-loop, some difference is noticeable between the nominal and extreme plant's response (Figure 4.3(b)). However, a very small difference. Again, as the uncertainty was only introduced in the transfer function from ΔRc to $\Delta\omega(s)$, and this transfer function has a low open loop gain (Figure 3.3(a)), the impact in the response is almost negligible. The Rc Variation and the impact it has on the angular speed, are presented in Figure 4.4.

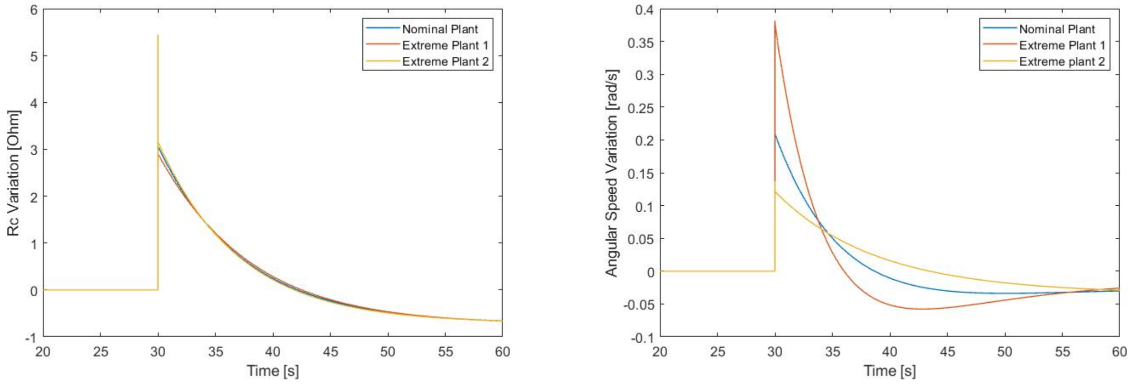

(a) Rc Variation.

(b) Rc Contribution to Angular Speed Variation.

Figure 4.4: Uncontrolled Closed-loop Rc.

In Figure 4.4(a) it can be seen that, in closed-loop, for a $4\,\mathrm{m/s}$ step input in the wind speed, the Rc only varies up to $5.5\,\Omega$. The result of this variation is presented in Figure 4.4(b), which shows that the impact from the ΔRc variation in $\Delta\omega$ is, in its maximum, $0.39\,\mathrm{rad/s}$. This magnitude, in angular speeds of around $6\,\mathrm{rad/s}$ is hardly noticeable, justifying the resemblance between open-loop and closed-loop uncontrolled responses.

Having a term for comparison, the test was performed for the controlled nominal plant, and for both extreme plants, the result is presented in the Figure 4.5(a).

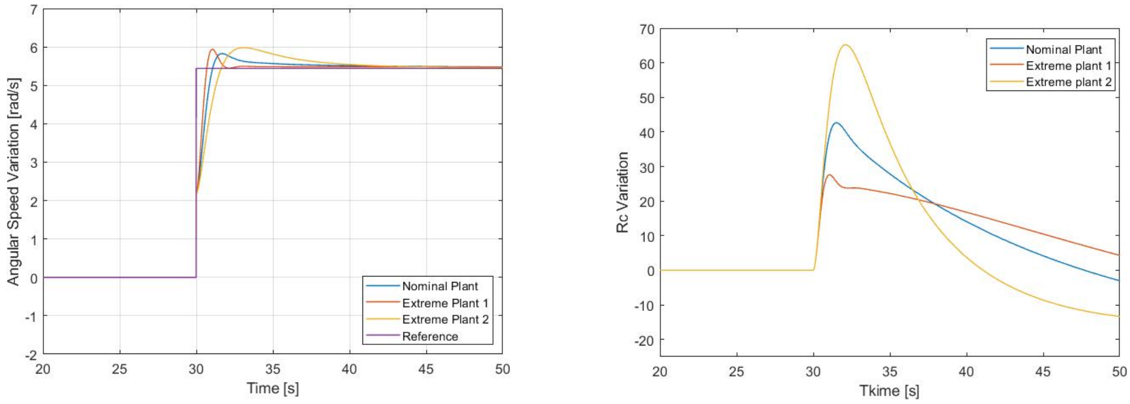

(a) Controlled Closed-Loop Response.

(b) Control Effort.

Figure 4.5: Closed-Loop Step Response - Step Input.

The angular velocity variation follows the reference needed to maintain the TSR at the optimum value, all three plants present a settling time lower than $10\,s$ and an overshoot of less than 10%, fulfilling the specifications. The control effort presented, shows that the load imposed resistance reaches values of around $200\,\Omega$, for the extreme plant 2.

The effect, the abrupt increase of the wind speed has on the TSR, can be observed in Figure 4.6.

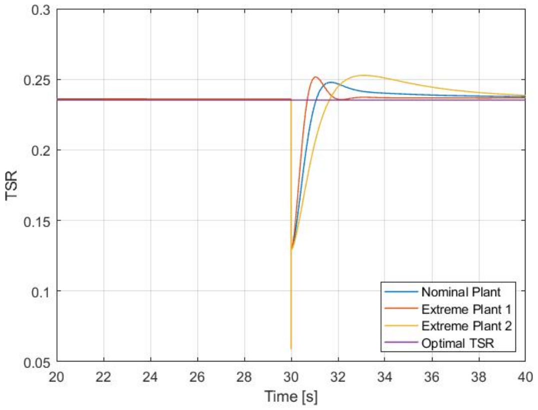

Figure 4.6: Tip Speed Ratio - Step Input.

The sudden change in the wind velocity causes a decrease in the TSR and consequently a decrease in the turbine's efficiency. The presence of the controller counteracts this effect, and in less than $10\,s$ the turbine's efficiency is again at it's maximum

4.1.2 With Turbulence

In this section different simulations were conducted. In order to maintain the conditions as real as possible, the step input was substituted for a smoother signal, and the turbulence present in a real wind stream was considered. The nominal wind speed before adding the turbulence is presented in Figure 4.7.

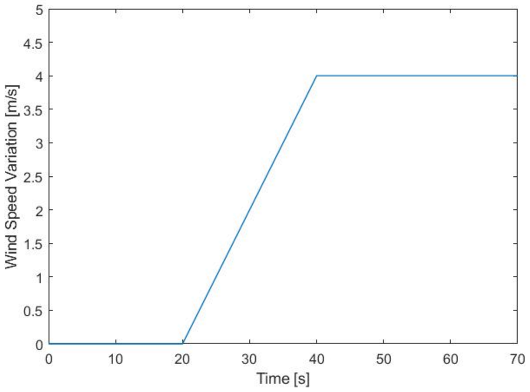

Figure 4.7: Nominal Wind Speed Variation.

The wind value from which is computed the optimal angular speed that maintains the TSR in the "optimal" value $\lambda = 0.2353$, is still the signal without turbulence (Figure 4.7), as in a real environment the signal from the anemometer would be filtered before the operation. Thus, the signal with turbulence will only be used as a disturbance, and not to compute the reference.

Turbulent Wind Model

In the present test, the wind input is modelled resorting to the turbulent wind model presented in section 2.3. Considering the nominal wind speed pictured in Figure 4.7, after adding the turbulence model, the wind speed signal is as presented in Figure 4.8.

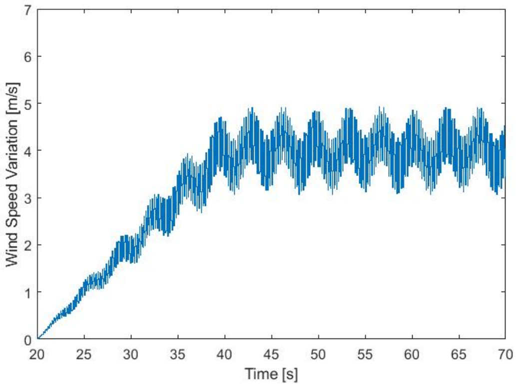

Figure 4.8: Wind Speed Variation with Turbulence.

For a cleaner observation, this simulation is only performed for the nominal plant, as the results from the three plants are lookalike, and overlap each other (Figure 4.9).

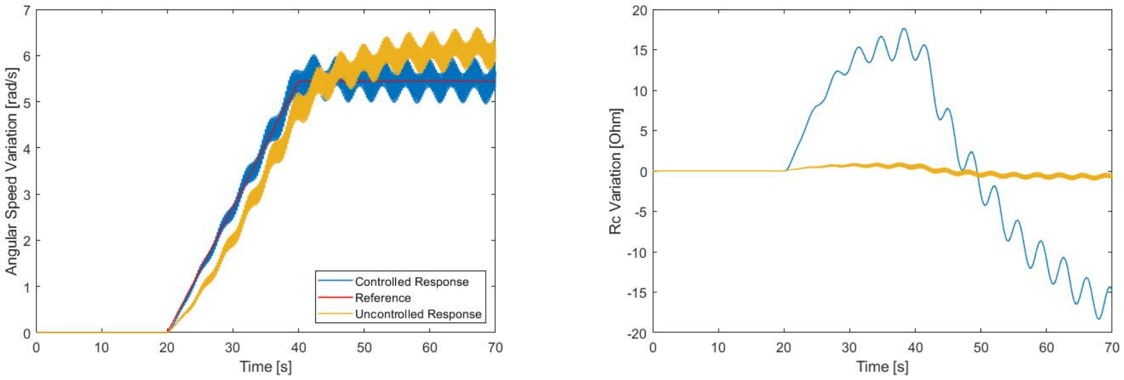

(a) Angular Speed Variation.

(b) Control Effort.

Figure 4.9: Controlled Closed-Loop Response - Harmonic Turbulence.

In Figure 4.9(a) it is shown that, despite the turbulence and the variation around the optimal angular speed, the system can track reasonably well the reference imposed by the variation of $4\,\mathrm{m/s}$ in the wind speed. The circuit imposed load has its maximum value of approximately $146\,\Omega$ for a $\Delta R_c \approx 15\,\Omega$. The comparison between the optimal TSR value, and the achieved one is presented in Figure 4.10.

The optimal TSR is depicted in red, while the TSR obtained with the CRONE control is presented in blue and the TSR obtained in closed-loop without any control action is depicted in yellow. It is obvious that there is an improvement when using the CRONE control. While the controlled response oscillates around the optimal TSR, the uncontrolled one is almost always far from the optimal point.

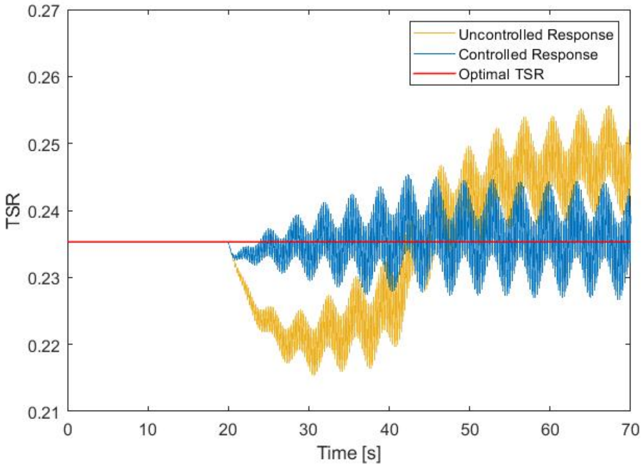

Figure 4.10: Tip Speed Ratio - Harmonic Turbulence

White Noise Model

In the present test, instead of the turbulent wind model used in the previous one, white noise was added to the wind speed sequence, in order to simulate a wind disturbance. This wind sequence is presented in Figure 4.11.

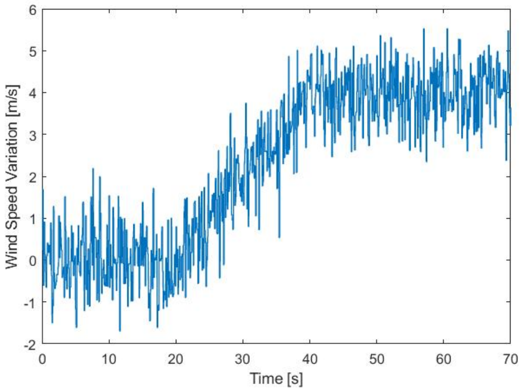

Figure 4.11: Wind Speed Variation with White Noise.

The controlled system's response as well as the control effort are presented in Figure 4.12.

It can be seen that the angular speed, in general, follows the reference, although not being able to counteract the fast changes in the wind speed. The transfer function from the input wind speed variation to the angular speed variation $\frac{\Delta v(s)}{\Delta \omega(s)}$ has a very fast dynamic due to the pole located at $s = -13200$, passing ahead all the ”noise” input that acts as output disturbance in the controlled plant. The real prototype should not react to the turbulent wind as fast as this model.

The TSR obtained during the simulation is presented in Figure 4.13.

From Figure 4.13 one can observe that the controlled behaviour presents an improvement relative to the uncontrolled response, the TSR maintains its value around the optimal point, however with some variation due to the turbulence considered.

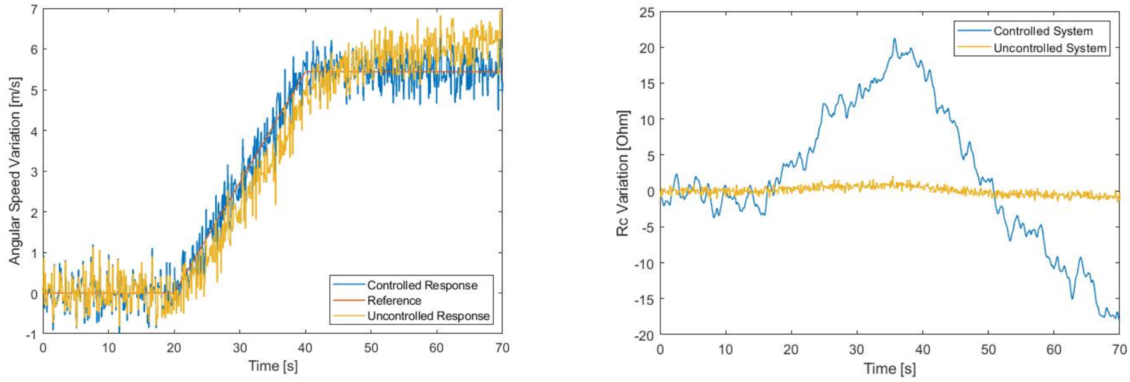

(a) Angular Speed Variation.

(b) Control Effort.

Figure 4.12: Controlled Closed-Loop Response - White Noise Turbulence.

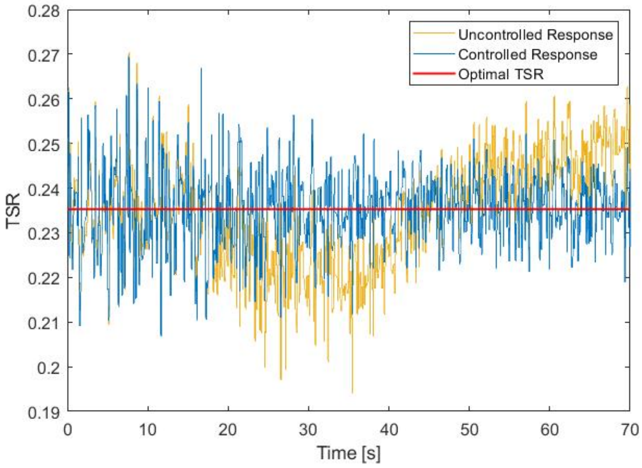

Figure 4.13: Tip Speed Ratio - White Noise Turbulence

4.1.3 Controller Performance Assessment

In order to evaluate the performance of the controller the following metrics were applied:

- the integral of time multiplied by the absolute value of the error (ITAE):

$$ITAE = \int_0^f t \cdot |e(t)|\, dt \tag{4.1}$$

- integral of the square value (*ISV*) of the control input:

$$ISV = \int_0^f u^2(t)\, dt \tag{4.2}$$

where ITAE is used as a numerical measure of tracking performance for the entire error curve, and ISV show the energy consumption of the control effort. The ITAE is a commonly used tracking performance metric in wind energy systems control problems. For example, this metric was used to assess and compare the controller's performance in [36] [20], [37] and [21]. The particularity of this measure is to weight errors that exists after a long time, more heavily than those at the start of the response. As for ISV, it is a measure that is also used in wind energy systems control, examples of that are [36], [20] and [21]. This a measure that is widely used, not only in wind energy systems, but in many control areas.

As in the case where the wind turbulent model is used, only appears turbulence from $20\,s$ on, the time frame taken into account is from $20\,\mathrm{s}$ to $70\,\mathrm{s}$ for the simulation with turbulent wind input. And for terms of comparison, in the white noise simulation the same time frame will be used. In the step input, only the simulation occurred after the step will be analysed. Table 4.1 to Table 4.3 summarize the performance assessment results for the different simulations.

Table 4.1: Step Input Simulation

	Nominal		Extreme 1		Extreme 2	
	Uncontrolled	*Controlled*	*Uncontrolled*	*Controlled*	*Uncontrolled*	*Controlled*
ITAE	797.594	27.76	802.747	32.133	796.198	19.855
ISV	38.702	14731	35.853	10102	39.439	22716

Table 4.2: Harmonic Turbulent Wind Simulation

	Nominal		Extreme 1		Extreme 2	
	Uncontrolled	*Controlled*	*Uncontrolled*	*Controlled*	*Uncontrolled*	*Controlled*
ITAE	695.116	265.064	694.251	256.437	698.469	271.769
ISV	17.129	6447.1	16.93	4680	17.368	8715.3

Table 4.3: White Noise Turbulent Wind Simulation

	Nominal		Extreme 1		Extreme 2	
	Uncontrolled	*Controlled*	*Uncontrolled*	*Controlled*	*Uncontrolled*	*Controlled*
ITAE	674.132	382.880	667.983	390.042	681.002	378.493
ISV	19.567	5746.6	18.937	4336.8	20.085	7955.4

It is important to note that this assessment does not intend to compare the performance of different controllers, as only one controller was synthesized, but to compare the performance of the same controller in different situations.

As expected, the step input simulation without turbulence is the easiest test to track, as the reference signal is simple and does not include any disturbances other than the wind step itself. However, is the test that requires a greater energy consumption, as the high amplitude abrupt change in the reference, has to be accompanied by a higher control effort. The test with the harmonic turbulence has a better tracking result than the one with white noise turbulence. This is achieved at a cost of a higher energy consumption, as the control effort in the white noise turbulence test is a slightly lower. In all tests, again as it was expected, the ITAE results are much better for the controlled system when compared to the closed-loop uncontrolled system.

When comparing the results between plants, one can observe that, the difference from the plant with the higher ITAE, to the one with the lower, never exceed 20, within the same test and for the controlled response. This particularity highlights the capability of the third generation CRONE controller, in positioning the uncertainty domains, in such a way that they have the smallest influence in the system's behaviour.

It is not possible to perform a comparison between the controller developed in this document and the ones developed in [7], as they were synthesised for different models and any comparison in simulation would be unfair. Therefore, an effort will be made in trying to compare the developed controllers when applied to the real system. This subject will be addressed in chapter 6.

4.2 Discrete-Time Simulation

All the tests performed above in continuous-time simulation were repeated in discrete-time simulation. The three plants were discretized as well as the controller developed. To implement the controller in the *Arduino*, and to be able to log the data in the computer, the transfer rate can not exceed $25\,\mathrm{Hz}$. Therefore the simulation sampling time was set to $T = 0.05\,\mathrm{s}$, to have a clearance of $0.01\,\mathrm{s}$. The transfer function $\frac{\Delta\omega(z)}{\Delta v(z)}$ is given by:

$$\frac{\Delta\omega(z)}{\Delta v(z)} = \frac{0.5473\,z - 0.5364}{z^2 - 0.993} \tag{4.3}$$

The nominal, extreme 1 and extreme 2 discretized plants are given by:

$$Nominal: \frac{\Delta\omega(z)}{\Delta Rc(z)} = \frac{0.07185\,z - 0.07185}{z^2 - 0.9993\,z}; \tag{4.4a}$$

$$Extreme\ 1: \frac{\Delta\omega(z)}{\Delta Rc(z)} = \frac{0.1287\,z - 0.1287}{z^2 - 0.9895\,z}; \tag{4.4b}$$

$$Extreme\ 2: \frac{\Delta\omega(z)}{\Delta Rc(z)} = \frac{0.03852\,z - 0.03852}{z^2 - 0.9953\,z}; \tag{4.4c}$$

4.2.1 Without Turbulence

Again, the controller was firstly tested using a step as wind perturbation, neglecting the turbulence present in the wind.

For this test, the wind is kept at its nominal value, assumed to be $v = 6\,m/s$ and at $t = 30s$ the disturbance is simulated as a step $\Delta v = 4\,m/s$. For $t \geq 10s$ the wind velocity is kept at its final value $v = 10\,m/s$. This test was performed for the nominal plant, and for both extreme plants.

For comparison purposes, as done in continuous-time simulation, all tests will be performed also in closed-loop without controller ($C = 1$). The results are presented in the Figure 4.14.

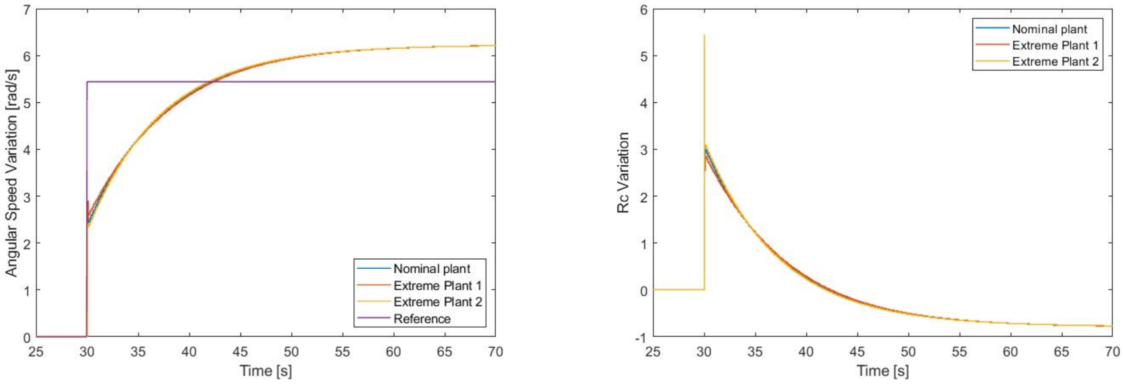

(a) Closed-Loop Response.

(b) Control Effort.

Figure 4.14: Closed-Loop Discrete Step Response ($C = 1$).

Following the results in continuous-time simulation, the uncontrolled closed-loop discrete-time response, presents a small difference between the plants. The results are consistent with the ones obtained in continuous-time, and the model presents the same behaviour.

The system was then tested in closed-loop with the discrete controller. The results for the angular speed variation and control effort can be seen in Figure 4.15

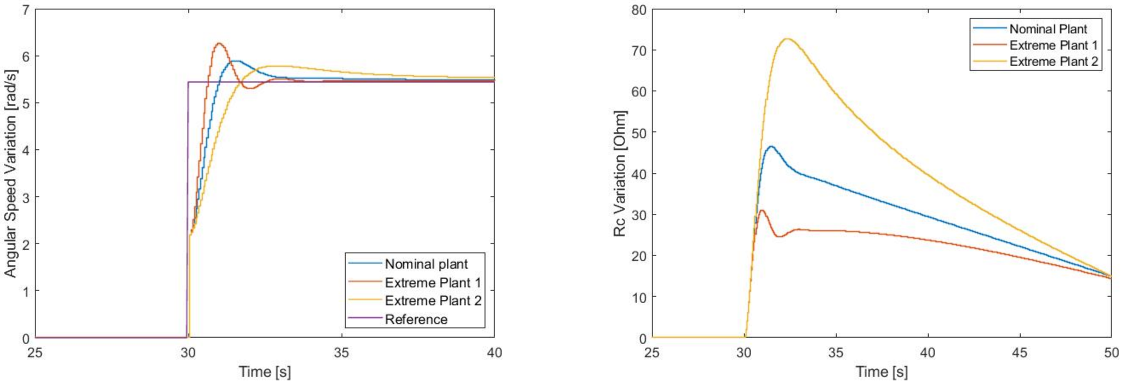

(a) Controlled Closed-Loop Response.

(b) Control Effort.

Figure 4.15: CRONE Controlled Discrete Closed-Loop Discrete - Step Input.

The discrete-time response presents an overshoot slightly bigger than the one in continuous-time. Although not exceeding the 20% defined by the specifications, even for extreme plant 1. The control effort in this test was also higher than the continuous-time, maintaining even though reasonable values; the higher resistance value in this test was approximately $Rc = 205\,\Omega$.

The effect on the TSR of the abrupt increase of the wind speed can be observed in Figure 4.16.

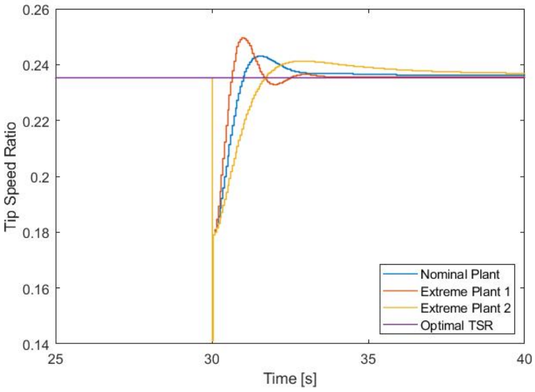

Figure 4.16: Tip Speed Ratio Discrete - Step Input.

The sudden change in the wind velocity causes a decrease in the TSR and consequently a decrease in the turbine's efficiency. The presence of the discrete controller counteracts this effect. Accompanying the higher overshoot observed in Figure 4.15(a), the discrete-time TSR also presents a higher overshoot than the continuous-one. The turbine is at its maximum efficiency, in less than $10\,\mathrm{s}$ after the step disturbance. This is valid for the nominal plant and for both extreme plants.

4.2.2 With Turbulence

In this section, the same test performed in section 4.1.2 is repeated in discrete-time. The nominal wind speed before adding the turbulence is the same as in the continuous-time simulation, and it is presented in f≪Figure 4.7.

The wind value from which is computed the optimal angular speed, to maintain the TSR in the ”optimal” value $\lambda = 0.2353$, is still the nominal value (without turbulence), similar to what was done in section 4.1.2.

Turbulent Wind Model

In the present test, the wind input is modelled resorting to the turbulent wind model presented in section 2.3. Once in real applications, the anemometer signal that is fed to the controller, is a discrete signal. Using the nominal wind speed pictured in Figure 4.7, the input signal is discretized.

For a cleaner observation, this simulation is only performed for the nominal plant, as the results from the three plants are lookalike, and overlap each other (Figure 4.17).

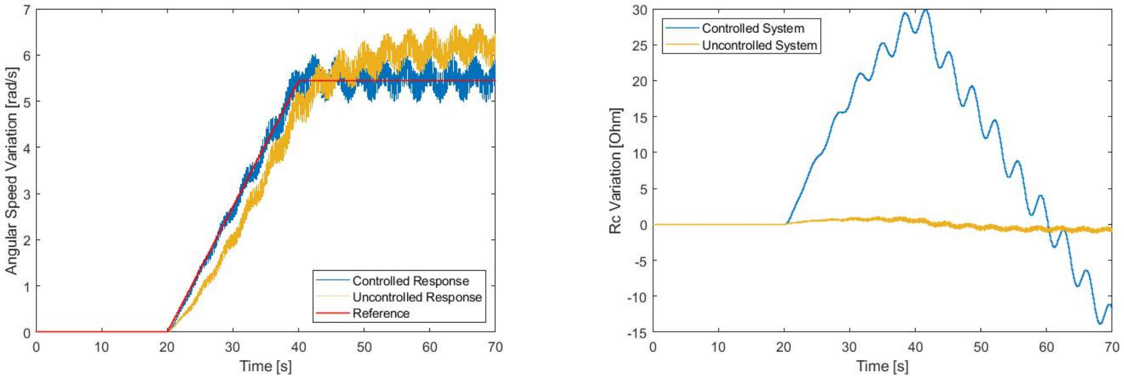

(a) Angular Speed Variation.

(b) Control Effort.

Figure 4.17: Discrete Closed-Loop Response - Harmonic Turbulence.

In Figure 4.17(a) is shown that, despite the turbulence and the variation around the optimal angular speed, the discrete controlled system can track reasonably well the reference when compared to the uncontrolled response. The circuit imposed load (Figure 4.17(b)) has its maximum value of $Rc \approx 176\,\Omega$, for a $\Delta Rc \approx 30\,\Omega$; twice as much as in the continuous-time simulation. The comparison between the optimal TSR value, the achieved one, and the uncontrolled is presented in figure 4.18.

The optimal TSR is depicted in red, while the TSR obtained with the CRONE control is presented in blue and the TSR obtained in closed-loop without any control action is depicted in yellow. It is easily observed that there is a significant improvement when using the CRONE controller.

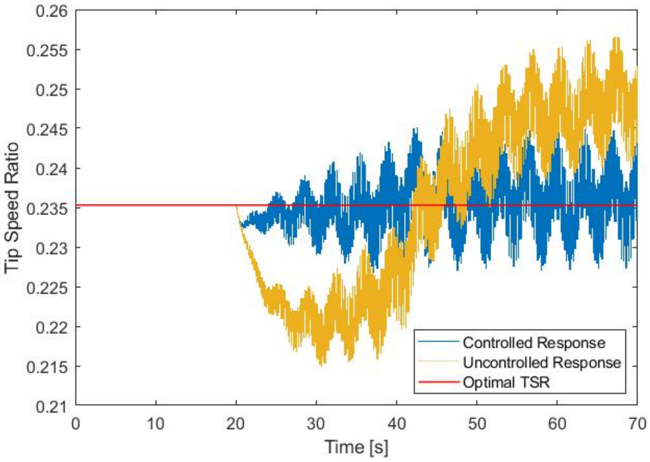

Figure 4.18: Tip Speed Ratio Discrete - Harmonic Turbulence.

White Noise Model

In the present test, instead of the turbulent wind model used in the previous one, white noise was added to the wind speed sequence in order to simulate a wind disturbance. The wind speed signal is based in the one presented in Figure 4.11, and discretized.

The systems response as well as the control effort are presented in Figure 4.19.

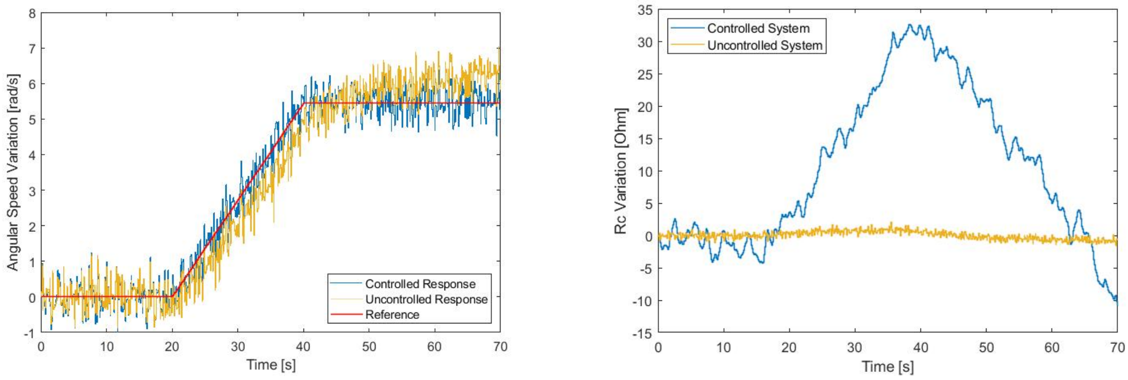

(a) Angular Speed Variation.

(b) Control Effort.

Figure 4.19: Discrete Closed-Loop Response - White Noise Turbulence.

It can be seen that the angular speed, in general, follows the reference. The results are similar to the ones obtained in continuous-time for the angular speed variation. In Figure 4.19(b) one can observe that the ΔRc reaches a value of around $35\,\Omega$, when in continuous-time, the maximum imposed load variation was of $20\,\Omega$. The controller needs to do a greater effort in discrete-time, to withstand the variances in angular speed that happen between actuations.

From Figure 4.20 one can observe that the controlled behaviour presents an improvement relative to the uncontrolled response, as happened in the continuous-time simulation.

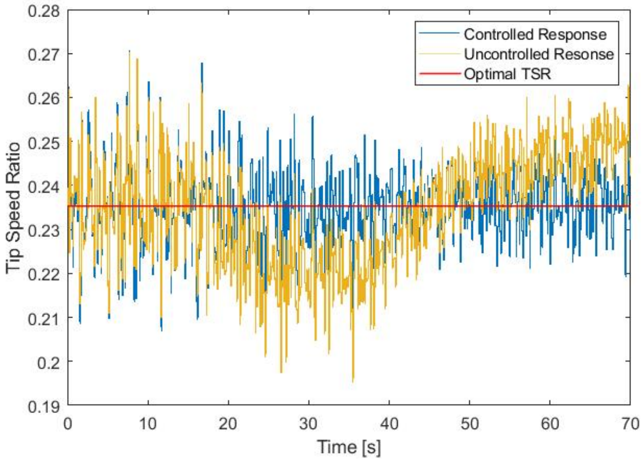

Figure 4.20: Tip Speed Ratio Discrete - White Noise Turbulence.

4.2.3 Controller Performance Assessment

In order to evaluate the performance of the controller, the same metrics applied in the continuous-time simulation were applied in discrete-time. The results obtained in the different tests are presented in Tables 4.4 to 4.6.

Table 4.4: Step Input Simulation

	Nominal		Extreme 1		Extreme 2	
	Uncontrolled	*Controlled*	*Uncontrolled*	*Controlled*	*Uncontrolled*	*Controlled*
ITAE	858.8	57.563	859.03	45.547	860.91	78.716
ISV	41.762	24120	40.714	13760	42.748	51189

Table 4.5: Harmonic Turbulent Wind Simulation

	Nominal		Extreme 1		Extreme 2	
	Uncontrolled	*Controlled*	*Uncontrolled*	*Controlled*	*Uncontrolled*	*Controlled*
ITAE	739.376	268.928	736.889	255.045	743.721	277.717
ISV	18.905	13381	18.687	8322.5	19.166	25882

The main objective of this comparison is to assess the performance of the system controlled and uncontrolled, and to compare the behaviour of the controller in different situations.

It can be seen that, in both the step input and the harmonic turbulence tests, the presence of the controller reduces to less than half, the tracking measurement ITAE. When comparing these results to the ones obtained in continuous-time simulation, both the ITAE and ISV for the controlled plants are higher in the present tests. The uncontrolled measurements are also higher in these tests, revealing that

Table 4.6: White Noise Turbulent Wind Simulation

	Nominal		Extreme 1		Extreme 2	
	$Uncontrolled$	$Controlled$	$Uncontrolled$	$Controlled$	$Uncontrolled$	$Controlled$
ITAE	716.1	391.875	711.203	406.089	721.665	387.097
ISV	21.416	13518	20.941	8489.3	21.836	25502

the discretization makes the system harder to control, as it was expected. The *ISV*'s, in the controlled situation, are in some tests the double of the ones achieved in the continuous-time tests,in line with the control effort observed in Figure 4.15(b), Figure 4.17(b) and Figure 4.19(b). Nonetheless, the results for the controlled response of the different plants, within the same test, are very close to each other. These results are consistent with the controller's ability to position the uncertainty domains, so that they have a minor influence in the system's response.

Chapter 5

Experimental Setup

In this chapter the experimental setup will be presented. The necessity to measure and manipulate physical quantities is common to all control and identification problems that move, beyond simulation, into the real world. Nowadays, pushed by the advance of technology and the massive entry of Asian manufacturers in the market, a large number of sensors and actuators, with considerable precision, have become common and cheap, along with a broad offer of microcontroller boards, that allow the integration of all components much more easily that it was a couple years ago.

All the hardware acquired or developed will be explained in detail, with the aim of being replicated, if needed, for further investigation in this prototype.

5.1 Intelligence

In order to gather all the signals from sensors and to command the actuators, while collecting data from the different variables at the same time, a platform was needed. There are several solutions in the market that could be used for this role, the *Raspberry Pi* boards, the *Teensy* boards or the *Arduino* family boards are only some examples of microcontroller platforms that suited the needs for this project. The choice fell to the *Arduino UNO* board(Figure 5.1), because it was already available in the laboratory, it has more than enough number of digital and analog I/O ports for this purpose, it is easy-to-use hardware and software, along with the capability of being used with *Matlab/Simulink* environment through a *Support Package* available in the *Mathworks* website [38].

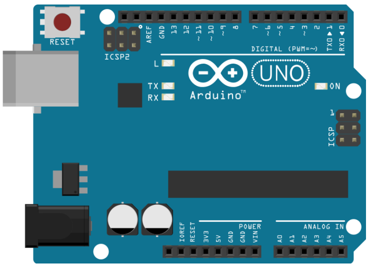

Figure 5.1: *Arduino UNO* Port Map.

The *Arduino UNO* is an open-source microcontroller board based on the *ATmega328P* microcontroller. The board is equipped with a total of 14 digital I/O pins (5 of them with PMW capabilities) and 6 analog *input* pins (Figure 5.1). The board can be programmed using the *Arduino IDE (Integrated Development Environment)* or using the *Simulink Support Package for Arduino* to create and run *Simulink* models on *Arduino*. The board can be powered via the USB cable, or by its power port, which admits between 7 to 20 volts, ensuring its standalone capabilities. The *Support Package* mentioned above also ensures a real-time communication between the *Arduino* board and the *Simulink* models running, allowing to monitor and record all the state variables for further analysis.

5.2 Sensors

In order to test and validate not only the controllers developed in the present document, but also the ones developed in [7], two main variables had to be measured in real-time: *Angular Speed* (ω) and *Wind Speed* (v). Beyond this two indispensable variables, two more are useful to understand and compare the controller's behaviour, and it was decided to measure both continuous current and tension output from the AC/DC converter. Both these physical quantities could easily be monitored making use of a multimeter or a *picoscope*. The choice of measuring them resorting to other equipment was made to easily integrate the data in the *Simulink* environment, and to be simpler to plot this data for a more straightforward visualization.

5.2.1 Angular Speed Sensor

For the angular speed measurement the choice was to use an infrared optical sensor. As studied in [6], the infrared sensor was the best option in this specific case when compared to two other sensor, namely a sonic sensor and a reed switch. Other possibilities were considered, but the infrared sensor was chosen for its simple implementation, low cost and enough precision for the purpose.

The basic infrared optical sensor includes an infrared high intensity LED and a photoresistor. There are two different ways of measuring the angular speed of a rotating body using an infrared sensor. The first, used in [6] and [7], and represented in Figure 5.2(a), consists of having the emitter and the photoresistor (represented in green) separated and, as an obstacle passes between them, it interrupts the beam. The second way is to use a reflective infrared optical Sensor, in which the emitter and the photoresistor are parallel to each other. In this situation, the photoresistor only receives a signal when an object passes at a limited distance in front of the sensor. In this type of setup there is no need for coupling another structure to a turbine's blade, and a higher precision can be achieved without increasing the number of structures to interrupt the beam, as the object in which the infrared beam is reflected can be each blade support (instead of having one interruption per turn, one can have five interruptions per turn, without having extra hardware). The solution adopted is represented in Figure 5.2(b).

The infrared sensor included in this project (Figure 5.3(a)) is capable of detecting obstacles at a distance that ranges from 2.5 to $10\,\mathrm{mm}$, therefore there is enough clearance for the turbine's vibrations

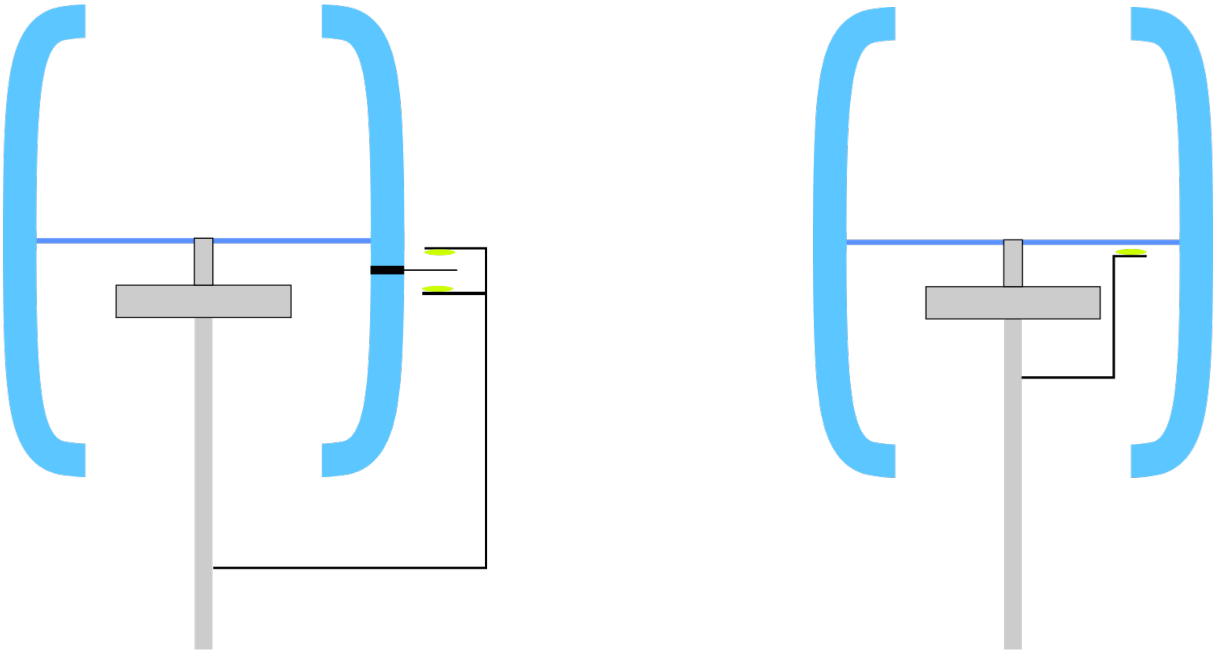

(a) Old Angular Speed Sensor Setup.

(b) New Angular Speed Sensor Setup.

Figure 5.2: Comparison Between the Old and New Angular Speed Sensor Setup.

(a) Reflective Infrared Optical Sensor.

(b) Infrared Sensor Setup.

Figure 5.3: Rotational Speed Sensor.

and looseness to occur without damaging the sensor or interfere with the measurements. It has also included a daylight blocking filter, allowing for it to be used in direct sunlight situations outdoors, unlike the one used in [6]. To secure the new infrared sensor in position, an aluminium support was built. The final configuration can be seen in Figure 5.3(b).

The sensor has three pins, Vcc, GND and $Signal$. These pins are connected to $5V$, $Ground$ and digital pin 3 in the *Arduino* respectively. It makes use of the *Arduino* function *interrupts()* specific for these cases when one cannot be dependent of the sampling time to catch the interruptions on the sensor. This function only works with digital pins 2 and 3 of *Arduino UNO*. For each interruption that the sensor detects, the *Arduino* records the time at which it occurred. Knowing the time between two consecutive interruptions, one can compute the turbine's angular velocity.

5.2.2 Wind Speed Sensor

The wind speed is an essential variable in this control problem, as together with the angular speed they are the only variables of the TSR function, the parameter that ultimately influences the turbine's efficiency. The hardware chosen to measure this physical quantity was a cup anemometer (Figure 5.4(a)) commercialized by *SparkFun* as part of weather station *kit*. The anemometer makes use of a reed switch (switch that closes in the presence of a magnetic field Figure 5.4(b)) and a neodymium magnet that closes the switch two times per revolution, again with the same method as explained above (section 5.2.1), it is possible to compute the angular velocity of the anemometer.

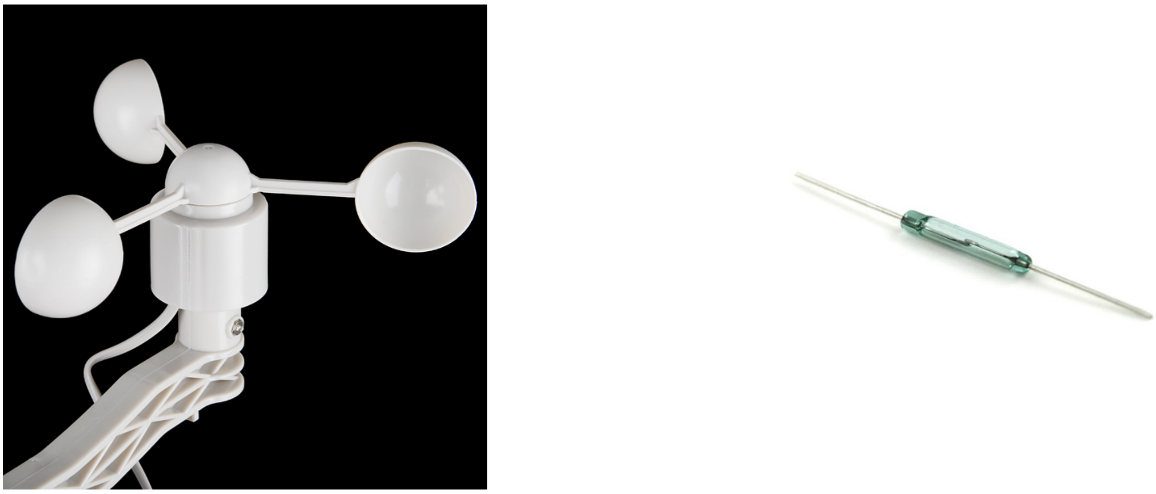

(a) *Sparkfun* Anemometer.

(b) Reed Switch.

Figure 5.4: Anemometer and Reed Switch.

The anemometer has two wires that are connected to both ends of the reed switch, one of the wires is to be connected to the *Arduino* pin 2 which supports the *interrupts()* function. This pin also has a *pull-up* resistor. Considering this, the best option is to connect the other wire to the *ground* pin, resulting in a signal that is usually 1, except when the neodymium magnet passes through the reed switch that it becomes 0. This strategy results in a signal similar to the one depicted in Figure 5.5.

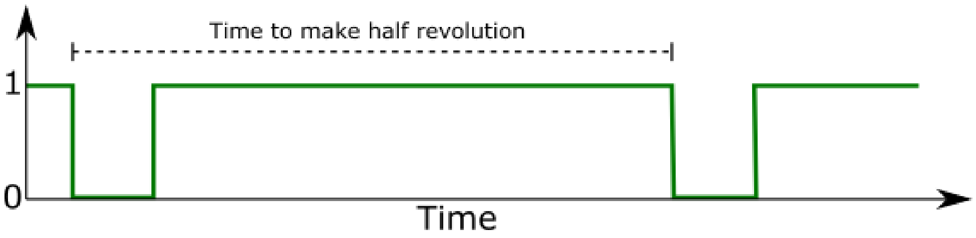

Figure 5.5: Anemometer Signal.

In the distributor's website can be found a guide [39] where is announced that, for this specific equipment: $1\ Rev/sec = 2.4\,\mathrm{km/h} = 0.666\,\mathrm{m/s}$, resorting to this conversion factor, the incident wind speed can be trivially computed.

5.2.3 Current and Voltage Sensors

In order to asses the power being produced by the PMSG, both current and voltage outputted by the AC/DC converter had to be monitored. Two simple circuits were implemented to achieve this objective

Tension Meter

The generator has a rated tension of $12V$ DC out of the AC/DC converter. As the analog pins from the *Arduino* only accept tensions up to $5V$, a voltage divider is needed. Its usual form is shown in Figure 5.6.

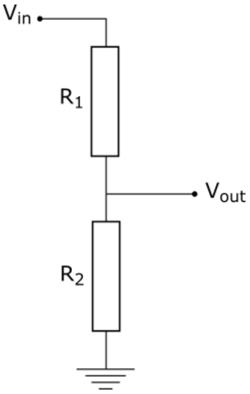

Figure 5.6: Voltage Divider Scheme.

This circuit allows to convert a signal between 0 and $12V$ to one between 0 and $5V$ by selecting the appropriate resistances R_1 and R_2. This circuit is characterized by the equation:

$$V_{out} = \frac{R_2}{R_1 + R_2} V_{in} \tag{5.1}$$

Selecting $R_1 = 6.8\,k\Omega$ and $R_2 = 4.7\,k\Omega$ a $V_{out} \approx 5\text{V}$ is achieved for a $V_{in} = 12\text{V}$. The V_{in} connects to the positive of the AC/DC converter, and the V_{out} wire connects to *Arduino* analog pin 1, the wiring scheme is shown in Figure 5.7. The *Arduino* analog pins have a $10 - bit$ resolution, meaning that with the voltage divider, the resolution in volts will be around 0.012V.

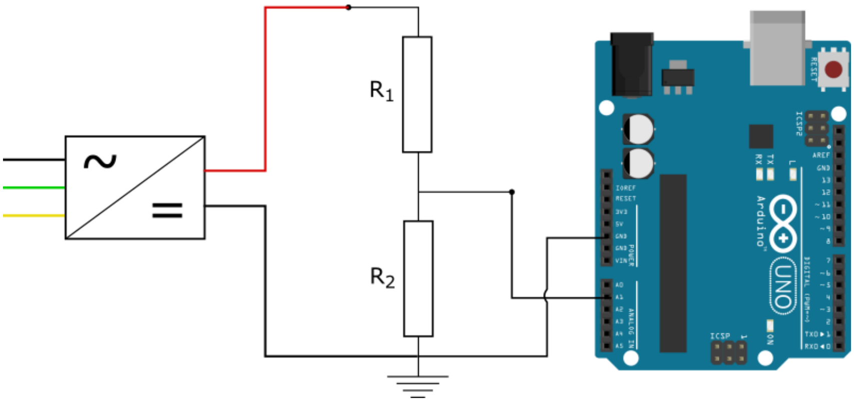

Figure 5.7: Voltage Divider Wiring Scheme Scheme.

Current Intensity Meter

According to the manufacturers (Appendix A), the PMSG has a rated power of $10W$, for a rated tension of $12V$, this translates into a rated current intensity of $\frac{10W}{12V} = 0.833A$. As the *Arduino* cannot measure current intensity, a current to voltage converter was implemented.

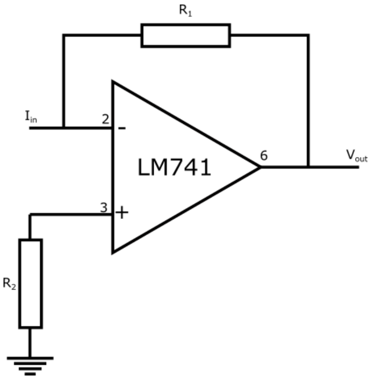

Figure 5.8: Current to Voltage Converter.

Resorting to an LM741 op-amp the circuit present in Figure 5.8 was designed. This circuit allows the tension out of the op-amp (V_{out}) to be proportional to current intensity (I_{in}) through the equation:

$$V_{out} = R_1\, I_{in} \tag{5.2}$$

Knowing that the *Arduino* can only measure tensions up to $5\mathrm{V}$ and assuming that the current intensity to be measured will not be greater than $1\mathrm{A}$, one can choose R_1 to maximize the resolution. This results in $R_1 = 5\Omega$, for a resolution of $\approx 1\,\mathrm{mA}$. The value of R_2 is the same as R_1 to keep errors to a minimum. The op-amp can be powered by the *Arduino*, resulting in the wiring scheme presented in Figure 5.9.

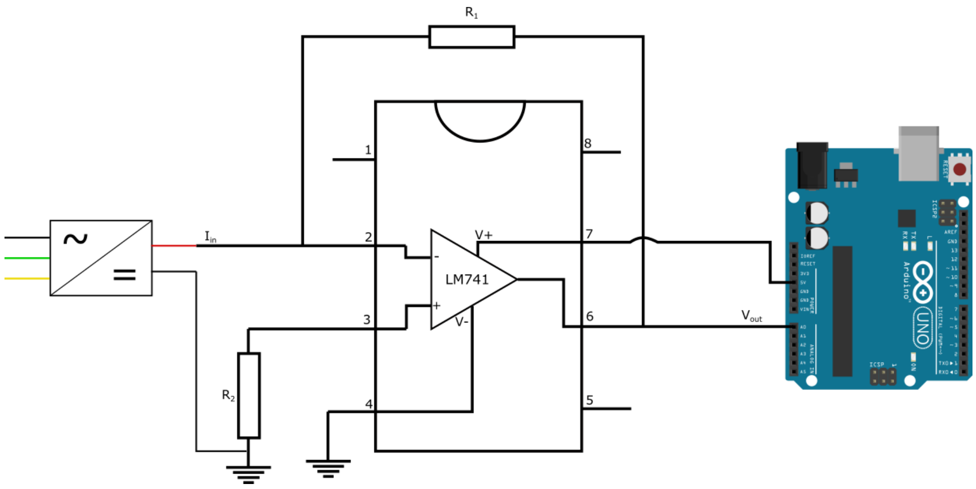

Figure 5.9: Current to Voltage Converter Wiring Scheme.

5.3 Actuators

In order to implement the control strategy, an automated way to manipulate the control variable Rc had to be created. In [7] the load applied to the PMSG was controlled manually resorting to three $100\,\Omega$ ceramic rheostats. This solution is suited for an identification process but not for control, where the resistive load has to be constantly adjusted precisely. The solution found was to attach one servo motor to each rheostat (Figure 5.10(a)), and have them commanded by the *Arduino* board. This is not an ideal solution, as the rotational range of the servo motor is shorter than the rheostat's. Instead of the original range from 0 to $100\,\Omega$ the actuator's range becomes limited from 0 to $80\,\Omega$. As a matter of versatility and to allow tests to be made with the PMSG in open-circuit, a relay module was included (Figure 5.10(b)). This device is a set of *Arduino* controlled switches, enabling the simulation of $Rc = inf$.

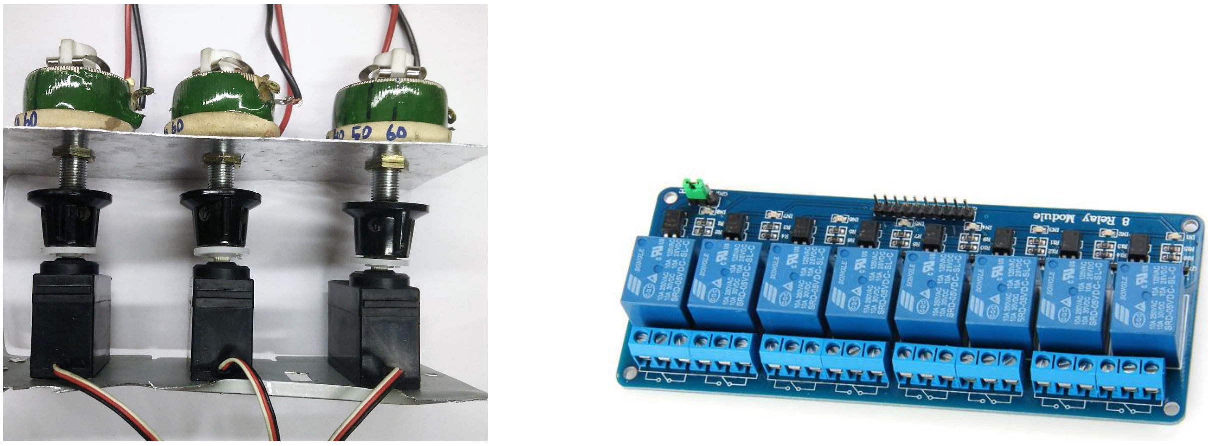

(a) Servo Motors and Rheostats Structure.

(b) Relay Module.

Figure 5.10: Actuator's Components.

Being the generator a 3-phase PMSG, the resistive loads are mounted in a Delta configuration as shown in Figure 5.11.

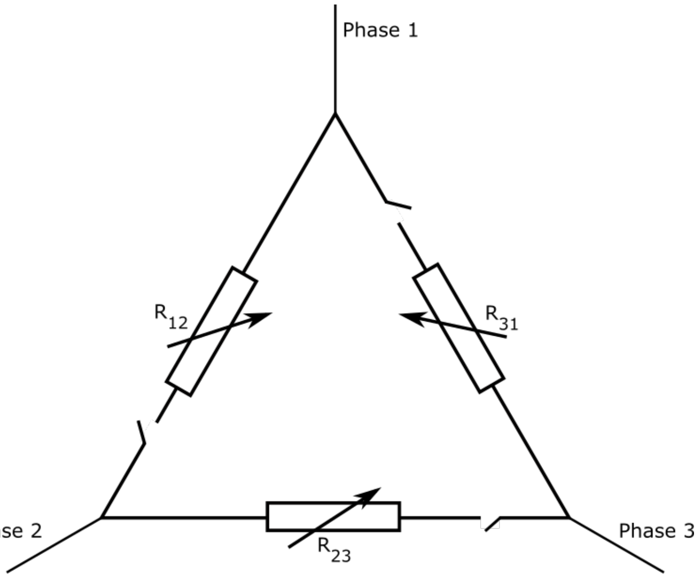

Figure 5.11: Circuit Scheme for Delta Configuration.

The servo motors have 3 wires, *Black*, *Red* and *White*. These stand for *Ground*, *5V* and *Signal* respectively. This standard servo motors are controlled by *Arduino* resorting to *PWM* (Pulse Width Modulation) feature of some digital pins, fortunately, there is a library included in the *Arduino IDE* (*Servo.h*). This library allows the user to input directly the degrees that wants the servo to rotate, avoiding more complex computation. The *Support Package* referred in 5.1 also has included *Simulink* blocks that allow a straightforward interaction with this devices.

Chapter 6

Experimental Results

In this chapter, the main objective was to validate the results obtained in simulation, with the developed controller. However, the software needed to read the data acquired by sensors, compute a response from the controller, and send it to the actuators couldn't be implemented in the *Arduino*. The developed routine uses more memory than the available in an *Arduino UNO*. Therefore, the controller developed was not tested in the prototype. The solution may be to acquire an *Arduino* model with more memory, or implement the software in a different type of platform.

Although the controller could not be tested, two tests in open loop were performed. The first test was intended to evaluate the prototype's TSR range, and to compare it to the maximum value proposed in section 2.2.1. And a second test, to evaluate the minimum and maximum TSR that could be achieved when using the actuators developed. The purpose of these tests, is to get to know the prototype's limits for control design purposes, and to have an idea of what rheostats to use when designing future actuators.

For both tests are presented, the raw data acquired from the sensors, and the low-pass filtered data.

6.1 Open-Loop Test Without Rheostat

In this first test, the objective was to acquire knowledge about the prototype's TSR range. The prototype was tested with the PMSG in both, open-circuit (infinite resistance) and short-circuit (zero resistance), resorting to the relay module installed. The test begins with the PMSG in open-circuit, and at $t = 200\,\mathrm{s}$ the circuit is closed. The wind stream was kept at a constant speed of around $6\,\mathrm{m/s}$ for the entire test. The results for the rotor angular speed obtained in this first test, are presented in Figure 6.1.

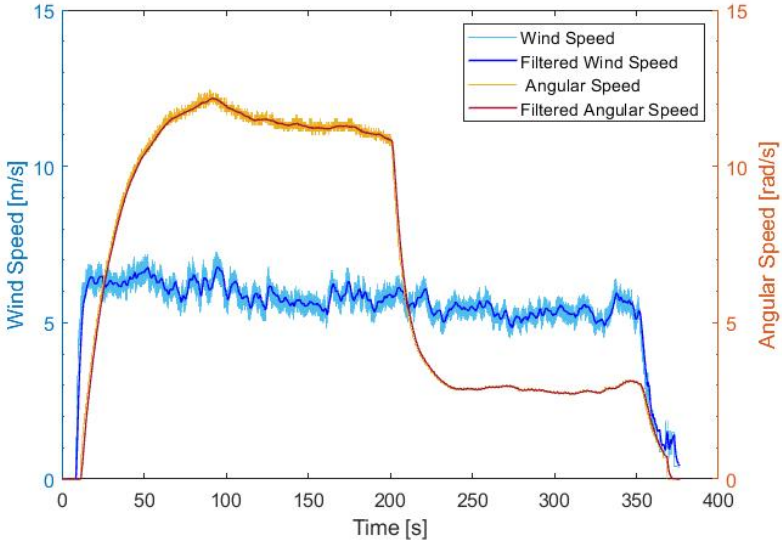

Figure 6.1: Wind Speed vs Rotor Angular Speed.

In Figure 6.1 it can be seen that, in open-circuit, the turbine takes almost $100\,\mathrm{s}$ to reach the steady state angular speed, presenting a small overshoot. Once in steady state, the rotor angular speed can be seen as constant, around $\omega = 11.5\,\mathrm{rad/s}$. When the circuit is closed, the angular speed drops $8.5\,\mathrm{rad/s}$, to around $3\,\mathrm{rad/s}$. The TSR evolution along this first test is presented in Figure 6.2.

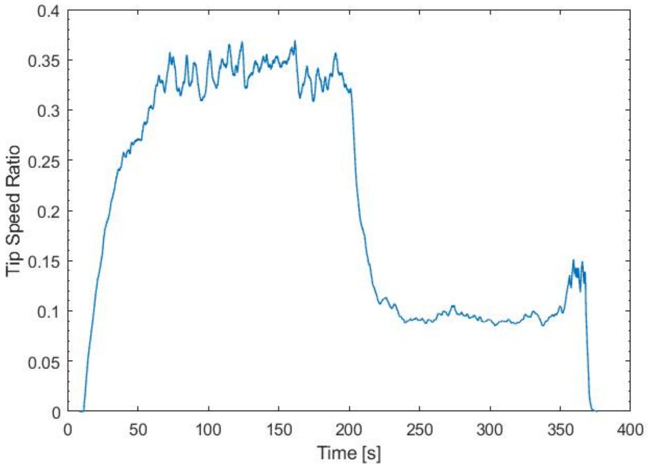

Figure 6.2: TSR Without Rheostat.

The results obtained in this test, are consistent with theoretical results from section 2.2.1. The maximum tip speed ratio presented by the prototype is around 0.35 in open-circuit. The minimum TSR, obtained with the PMSG in short-circuit is around 0.1. Placing the steady state TSR in the $[0.1; 0.35]$ interval.

6.2 Open-Loop Test With Rheostat

In this second test, the objective was to assess the TSR range available when introducing the rheostats as actuators. The variable resistances installed have an actuation range of 80Ω, from 0 to 80Ω. An offset can be added as a resistance in series with the rheostats, but for this test no offset was added.

The present test was conducted similar to the previous one, the wind speed was increased to approximately $6\,\mathrm{m/s}$, and kept at that value until $t = 250\,\mathrm{s}$. The resistance is at $80\,\Omega$, from the beginning of the test until $t = 150\,\mathrm{s}$, when it is changed for $0\,\Omega$ until the end of the test. The wind speed and rotor angular speed values are presented in Figure 6.3.

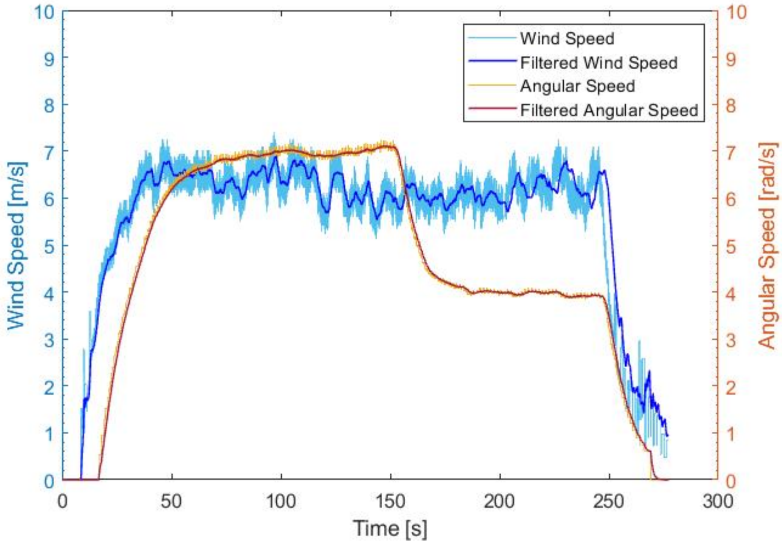

Figure 6.3: Anemometer Signal.

The results show that the angular speed, when the actuator is in the upper limit of its range, is smaller in $5.5\,\mathrm{rad/s}$ when compared with the test in open-circuit. The low wind self-start capability, is also compromised. The prototype initiates its movement for a higher wind speed than in the first test. In Figure 6.4 is presented the TSR evolution that resulted from this test.

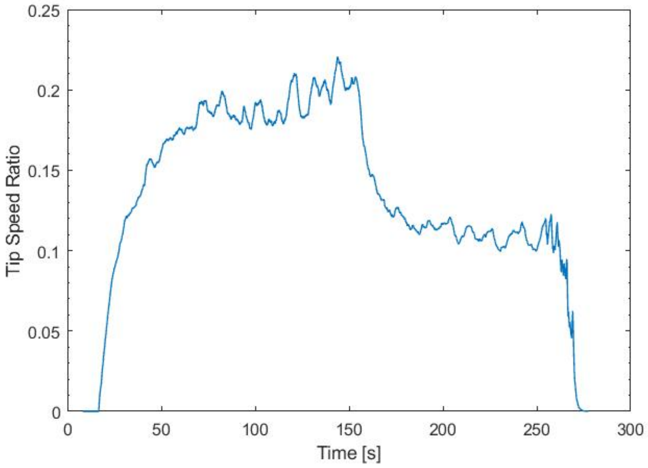

Figure 6.4: TSR With Rheostat.

The tip speed ratio obtained in this second test, has a maximum value of approximately 0.2, contrasting with the value of 0.35 obtained in the first test. The minimum value is again placed around 0.1, as the smallest resistance value of $0\,\Omega$ was kept constant between tests. The small range presented by the rheostat installed, limits the prototype's TSR to less than half its range. For control purposes, a larger actuation range provides more room to manipulate the turbine's behaviour. Therefore, in a future implementation, rheostats with a higher range should be installed.

Chapter 7

Conclusions

7.1 Achievements

In this document a Darrieus VAWT prototype is studied. Real and simulation data from previous projects are analysed, and considerations are made. It was proven that, the maximum tip speed ratio possible to be achieved by this prototype, with this PMSG, is around 0.353; far from the $\lambda_{opt} = 7$, used in previous work.

Five models developed in [7] were analysed, and the one that presents a response closer to the prototype's behaviour, is selected for control development. The selected MISO identified model was thoroughly studied and analysed, and used as the nominal plant that describes the prototype. Two types of uncertainties were studied and simulated: uncertainty in the transfer function's coefficient, and uncertainty in the zeros and poles location. After the observation, in the Nichols chart, of the uncertainty domains, the uncertainty in the transfer function's coefficients was used, and $\pm 20\%$ of uncertainty was added to the model.

A fractional third generation CRONE control was successfully developed resorting to the CRONE CSD Toolbox. The fractional controller was approximated to a rational one, in order to be applied in Matlab/Simulink simulation.

Three different disturbances were used to test the controller in a simulation environment: a step, a modelled harmonic turbulent wind, and white noise turbulent wind. The results obtained for both continuous and discrete-time simulations are similar, with the latest requiring a greater control effort for each disturbance, while presenting a slightly larger tracking error. In general, the controlled system has a tracking performance (ITAE) twice as good as the system's response without controller ($C = 1$). The CRONE controller has a good performance when it comes to overcome the differences between the nominal plant and perturbed one's. The metrics used to assess the controller performance do not present significant difference between plants, within the same test, despite the presence of the $\pm 20\%$ uncertainty in the controlled transfer function.

A set of sensors and an automated actuator were developed, and integrated with the *Arduino* platform. The software needed to read the sensors data, compute the controller's response and send it to the actuator was also produced. However, the control loop could not be implemented due to *Arduino's* lack of memory, miscalculated when deciding the platform to be used. Still, some experimental tests were performed, with the aim of confirming the prototype's TSR limits, obtained theoretically. Placing the TSR between 0.35 and 0.1, and confirming the results obtained in chapter 2. Another test was conducted, to assess the limitations that the range of the actuator would impose to the behaviour of the prototype. This test led to the conclusion that, with the actuators installed, the range of the prototype's TSR would be reduced to less than half, from $[0.35, 0.1]$ to $[0.2, 0.1]$.

7.2 Future Work

During the project, it was found that the model selected does not represent accurately the behaviour of the prototype. The curve $C_p(\lambda)$ proposed in previous works is not consistent with the results obtained experimentally. An effort should be done to obtain an experimental curve, and a new theoretical model should be developed, based on this new curve.

As stated in chapter 6, a new platform with more memory should be acquired to implement the control loop in order to test not only the controller developed in the present document, but also to compare it with the controllers developed in [7]. For this new implementation, the servo-motors should be replaced by stepper-motors and the rheostats replaced by ones with a wider range, or, instead, a digital potentiometer should be used.

Regarding the general prototype control, to have a wider wind range operation, a state machine should be developed, along with different controllers for the different wind conditions.

Bibliography

[1] R. Carter. The neolithic origins of seafaring in the arabian gulf. *Archaeology International*, 6:44–47, 2002. doi: 10.5334/ai.0613.

[2] GWEC. Global wind report - anual market update. Technical report, Global Wind Energy Council, 2017.

[3] K. R. Haapala and P. Prempreeda. Comparative life cycle assessment of 2.0 mw wind turbines. *International Journal of Sustainable Manufacturing*, 3(2):170–185, Jan 2014. doi: 10.1504/IJSM.2014.062496.

[4] N. C. Batista, R. Melício, V. M. F. Mendes, M. Calderón, and A. Ramiro. On a self start darrieus wind turbine; blade design and field tests. *Renewable and Sustainable Energy Reviews*, 52:508–522, Dec 2015. doi: 10.1016/j.rser.2015.07.147.

[5] H. Sintra, V. M. F. Mendes, and R. Melício. Modeling and simulation of wind shear and tower shadow on wind turbines. In *Procedia Technology*, volume 17, pages 471–477, Dec 2014. doi: 10.1016/j.protcy.2014.10.255.

[6] N. Batista. *Novo Aerogerador de Eixo Vertical Integrado Numa Rede Inteligente em Contexto Urbano*. PhD thesis, Universidade de Évora, 2013.

[7] T. R. Pereira. Control development for a darrieus prototype integrated in a smartgrid for urban context. Master's thesis, Técnico Lisboa - Universidade de Lisboa, 2017.

[8] W. Tjiu, T. Marnoto, S. Mat, and M. Ha. Darrieus vertical axis wind turbine for power generation I: Assessment of Darrieus VAWT configurations. 75:50–67, 2015. doi: 10.1016/j.renene.2014.09.038.

[9] F. Balduzzi, A. Bianchini, E. A. Carnevale, L. Ferrari, and S. Magnani. Feasibility analysis of a Darrieus vertical-axis wind turbine installation in the rooftop of a building. *Applied Energy*, 97:921–929, Sept 2012. doi: 10.1016/j.apenergy.2011.12.008.

[10] G. Müller, M. F. Jentsch, and E. Stoddart. Vertical axis resistance type wind turbines for use in buildings. *Renewable Energy*, 34:1407–1412, May 2009. doi: 10.1016/j.renene.2008.10.008.

[11] W. T. Chong, S. C. Poh, A. Fazlizan, and K. C. Pan. Vertical axis wind turbine with omni-directional-guide-vane for urban high-rise buildings. *Journal of Central South University*, 19:727–732, Mar 2012.

[12] N. Batista, R. Melício, V. M. F. Mendes, and J. Figueiredo. Wireless Monitoring of Urban Wind Turbines by ZigBee Protocol : Support Application Software and Sensor Modules. *Procedia Technology*, 17:461–470, 2014. doi: 10.1016/j.protcy.2014.10.182.

[13] N. Batista, R. Melício, J. C. O. Matias, and J. P. S. Catalão. New Blade Profile for Darrieus Wind Turbines Capable to Self Start. pages 1–5. IET Conference on Renewable Power Generation (RPG 2011), Sept 2011. doi: 10.1049/cp.2011.0219.

[14] N. C. Batista, R. Melício, and V. M. F. Mendes. Darrieus-type vertical axis rotary-wings with a new design approach grounded in double-multiple streamtube performance prediction model. *AIMS Energy*, 6:673–694, Sept 2018. doi: 10.3934/energy.2018.5.673.

[15] N. Batista, R. Melício, and J. Catalão. ”pás de forma ajustável para turbinas de rotor vertical”, . Patente PT 105445, pedido provisório de patente efectuado em 22 de dezembro de 2010, registo definitivo: Boletim de Propriedade Industrial N^o 119/2012, 05 de junho de 2013.

[16] N. Batista, R. Melício, and J. Catalão. ”vertical axis turbine blades with adjustable form”, . Patent US 2012/0163976a1, provisional patent application made in 20 december 2011, final registration Pub. N^o us 2012/0613976, 28 june 2012.

[17] T. Pereira, N. Batista, A. Fonseca, C. Cardeira, P. Oliveira, and R. Melicio. Darrieus wind turbine prototype: Dynamic modeling parameter identification and control analysis. *Energy*, 159:961–976, Sep 2018. doi: 10.1016/j.energy.2018.06.162.

[18] R. Melício, V. M. F. Mendes, and J. P. S. Catalão. Fractional-order control and simulation of wind energy systems with PMSG/ full-power converter topology. *Energy Conversion and Management*, 51:1250–1258, Jun 2010. doi: 10.1016/j.enconman.2009.12.036.

[19] M. Andriollo, M. D. Bortoli, G. Martinelli, A. Morini, and A. Tortella. Control strategies for a VAWT driven PM synchronous generator. pages 804–809. IEEE, Jun 2008. doi: 10.1109/SPEEDHAM.2008.4581124.

[20] C. Viveiros, R. Melício, J. Igreja, and V. M. F. Mendes. Performance assessment of a wind energy conversion system using a hierarchical controller structure. *Energy Conversion and Management*, 93:40–48, Mar 2015. doi: 10.1016/j.enconman.2015.01.002.

[21] C. Viveiros, R. Melicio, V. Mendes, and J. Igreja. Adaptive and predictive controllers applied to onshore wind energy conversion system. *AIMS Energy*, 6(4):615–631, 2018. doi: 10.3934/energy.2018.4.615.

[22] T. Marques. Control and operation of a vertical axis wind turbine, June 2014.

[23] A. Oustaloup. La Commande CRONE. *Commande Robuste d'Ordre Non Entier*, (6):130–135, 1991.

[24] A. Oustaloup, B. Mathieu, and P. Lanusse. Second generation CRONE control. In *Proceedings of IEEE Systems Man and Cybernetics Conference - SMC*, pages 136–142. IEEE, 1993. ISBN 0-7803-0911-1.

[25] P. Lanusse, A. Oustaloup, and B. Mathieu. Third generation CRONE control. In *Proceedings of IEEE Systems Man and Cybernetics Conference - SMC*, pages 149–155. IEEE, 1993. doi: 10.1109/ICSMC.1993.384864.

[26] A. Oustaloup, B. Mathieu, and P. Lanusse. The CRONE Control of Resonant Plants: Application to a Flexible Transmission. *European Journal of Control*, 1:113–121, Jan 1995. doi: 10.1016/S0947-3580(95)70014-0.

[27] P. Lanusse, R. Malti, and P. Melchior. CRONE control system design toolbox for the control engineering community: tutorial and case study. *Philosophical Transactions of the Royal Society*, (371), Apr . doi: 10.1098/rsta.2012.0149.

[28] *CRONE Control Design Module User's Guide*. CRONE Research Group, version 4.0 edition, Oct 2010.

[29] P. Lanusse, M. Lopes, J. Sabatier, and B. Feytout. New optimization criteria for the simplification of the design of third generation CRONE controllers. *IFAC Proceedings Volumes*, 46(1):355–360, Feb 2013. doi: 10.3182/20130204-3-FR-4032.00074.

[30] R. Melício. *Modelos Dinâmicos de Sistemas de Conversão de Energia Eólica Ligados à Rede Eléctrica*. PhD thesis, Universidade da Beira Interior, 2010.

[31] A. Betz. *Das maximum der teoretisch möglichen ausnützung des windes durch windmotoren*. *Int. J. Zeitschrift für das Gesamte Turbinewesen*, 26:307–309, 1920.

[32] R. Melício, V. M. F. Mendes, and J. P. S. Catalão. Wind Turbines with Permanent Magnet Synchronous Generator and Full-Power Converters: Modelling, Control and Simulation. In *Wind Turbines*, pages 465–494. InTech, 2011.

[33] J. F. Manwell, J. G. McGowan, and A. L. Rogers. *Wind Energy Explained: Theory, Design and Application*. John Wiley & Sons, 2 edition, 2010. ISBN 978-0-470-01500-1.

[34] J. Sabatier, P. Lanusse, P. Melchior, and A. Oustaloup. *Fractional Order Differentiation and Robust Control Design*, volume 77 of *Intelligent Systems, Control and Automation: Science and Engineering*. Springer Netherlands, 2015. ISBN 978-94-017-9806-8.

[35] B. Mathieu. *De la commande CRONE scalaire à la commande CRONE multivariable*. PhD thesis, Université Bordeaux, 1997.

[36] C. Viveiros, R. Melício, J. M. Igreja, and V. M. F. Mendes. Fractional order control on a wind turbine benchmark. *System Theory, Control and Computing (ICSTCC), 2014 18th International Conference*, pages 76–81, 2014. doi: 10.1109/ICSTCC.2014.6982394.

[37] Y. Tang, Y. Bai, C. Huang, and B. Du. Linear active disturbance rejection-based load frequency control concerning high penetration of wind energy. *Energy Conversion and Management*, 95: 259–271, 2015. doi: 10.1016/j.enconman.2015.02.005.

[38] https://www.mathworks.com/hardware-support/arduino-simulink.html. Downloaded in 26/05/2018.

[39] https://learn.sparkfun.com/tutorials/weather-meter-hookup-guide. Visited in 29/08/2018.

Appendix A

SAV-15W Brochure

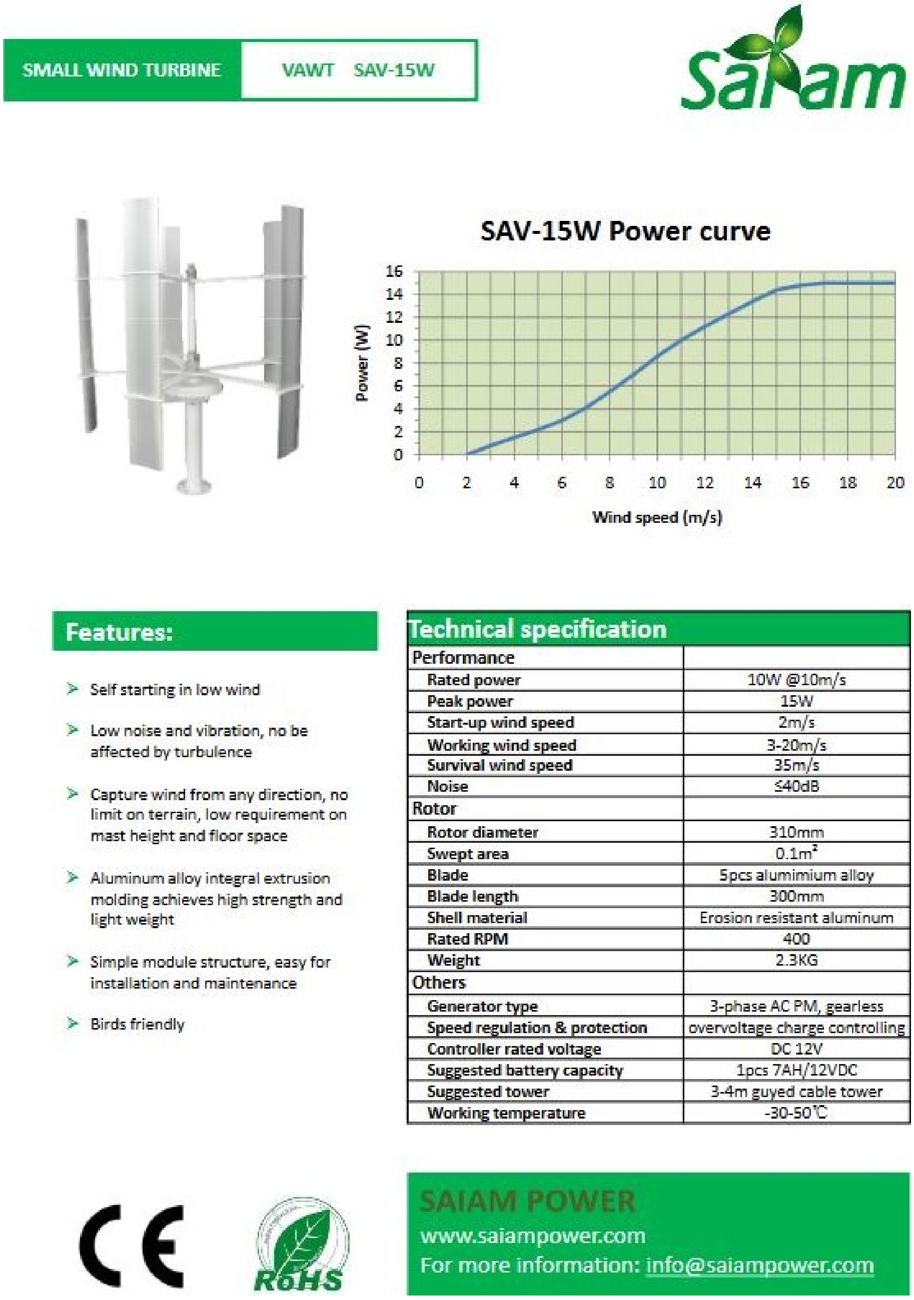

SMALL WIND TURBINE | VAWT SAV-15W

Features:

- Self starting in low wind
- Low noise and vibration, no be affected by turbulence
- Capture wind from any direction, no limit on terrain, low requirement on mast height and floor space
- Aluminum alloy integral extrusion molding achieves high strength and light weight
- Simple module structure, easy for installation and maintenance
- Birds friendly

Technical specification	
Performance	
Rated power	10W @10m/s
Peak power	15W
Start-up wind speed	2m/s
Working wind speed	3-20m/s
Survival wind speed	35m/s
Noise	≤40dB
Rotor	
Rotor diameter	310mm
Swept area	0.1m²
Blade	5pcs alumimium alloy
Blade length	300mm
Shell material	Erosion resistant aluminum
Rated RPM	400
Weight	2.3KG
Others	
Generator type	3-phase AC PM, gearless
Speed regulation & protection	overvoltage charge controlling
Controller rated voltage	DC 12V
Suggested battery capacity	1pcs 7AH/12VDC
Suggested tower	3-4m guyed cable tower
Working temperature	-30-50℃

SAIAM POWER
www.saiampower.com
For more information: info@saiampower.com